

Chapter 5

Optimal placement of actuators and sensors

In the implementation of a controller, actuators and sensors are needed. The locations of actuators and sensors over a structure determine the effectiveness of the controller in controlling vibrations. If we wish to control a particular vibration mode, we need to place actuators and sensors in locations with high control and observation authority over that mode. In many cases of vibration control, low frequency modes are considered to be important. Hence, we only need to consider a certain number of modes in the placement of actuators and sensors. This implies that we need to place actuators and sensors in locations where the controllability and observability of some modes are sufficiently high.

Another issue to consider in the placement of actuators and sensors is the control and observation spillover. In control design, only a number of low frequency modes are of interest, so the high frequency modes are often neglected. However, actuators or sensors may excite or observe some high frequency modes that may damage the closed-loop stability and performance. If actuators or sensors are placed at locations where they have large authority over some high frequency modes, the spillover effect will be more significant. It is thus important to place actuators or sensors at locations where one has less authority to control or observe high frequency modes, so as to minimize the effect of spillover.

In this chapter, the optimal placement of actuators and sensors based on the notion of spatial \mathcal{H}_2 norm is discussed. Our approach is to treat the optimal placement of actuators and sensors independently, and the optimization is also independent of controllers to be used. This approach can be useful when more than one controller type is to be tested on the structure and when it is impractical to remove or replace the actuators and sensors used. Hence, different controllers may be tested on the structure to compare their performances. In particular, optimal placement of piezoelectric actuators and sensors over a plate structure will be discussed.

5.1 Modelling of piezoelectric laminate plates

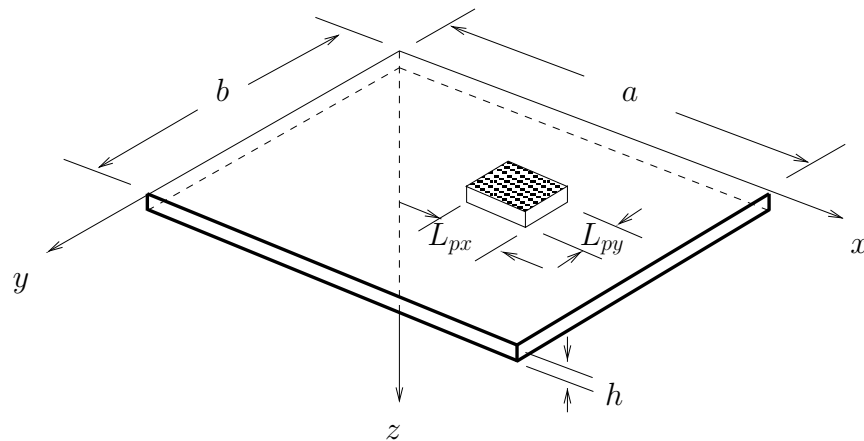


Figure 5.1: A plate with the j^{th} piezoelectric patch attached

Consider a thin uniform plate with dimensions of $a \times b \times h$ as shown in Figure 5.1. In Chapter 2, the PDE for flexure vibration of thin plates was derived (2.37):

$$\rho h \frac{\partial^2 w}{\partial t^2} + D \nabla^4 w(x, y, t) = \frac{\partial^2 M_{px}}{\partial x^2} + \frac{\partial^2 M_{py}}{\partial y^2}$$

where all parameters were defined in Section 2.1.4.

Suppose there are J actuators distributed over the plate. The right-hand-side term of the PDE is the external moment per unit length that may be generated

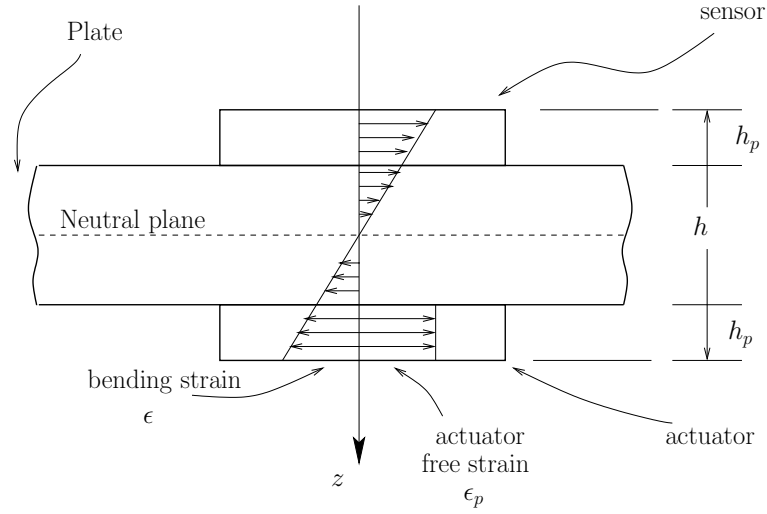


Figure 5.2: A plate section with piezoelectric patches attached

by piezoelectric actuators. The forcing term contributed by all actuators is represented by

$$\frac{\partial^2 M_{px}}{\partial x^2} + \frac{\partial^2 M_{py}}{\partial y^2} = \sum_{j=1}^J \alpha_j V_{aj}(t) \quad (5.1)$$

where V_{aj} is the input signal to the j^{th} actuator. The term α_j depends on the properties and location of the j^{th} actuator.

We now consider a particular case of using piezoelectric patches as actuators. Consider J rectangular piezoelectric actuators attached to a rectangular plate. All actuator patches are oriented in the same direction as the plate. Now, the derivation for a one-dimensional case in Chapter 2 is extended to two-dimensional structures [DFR91, FEN96]. Consider the j^{th} piezoelectric actuator of dimensions $L_{px} \times L_{py} \times h_p$ in Figure 5.1. Let us assume that all the properties described below belong to the j^{th} actuator. Again, we assume negligible contribution of patches to the overall mass and stiffness properties of the structure since the patches are relatively thin.

The free strains generated inside the patch due to applied voltage V_{aj} are [FEN96, BSW96]

$$\begin{aligned}\epsilon_{px} &= \left(\frac{d_{31}}{h_p}\right) V_{aj}(t) \\ \epsilon_{py} &= \left(\frac{d_{32}}{h_p}\right) V_{aj}(t)\end{aligned}\quad (5.2)$$

where the piezoelectric charge constants along x and y axes are denoted by d_{31} and d_{32} respectively.

The strains acting on the structure are the bending strains, ϵ_x and ϵ_y , and the free strains, ϵ_{px} and ϵ_{py} , as shown in Figure 5.2. The longitudinal stresses acting inside the actuator in x and y directions, σ_{px} and σ_{py} , can be found from Hooke's law for plane stress:

$$\begin{aligned}\sigma_{px} &= \frac{E_p}{1 - \nu_p^2} (\epsilon_x - \epsilon_{px} + \nu(\epsilon_y - \epsilon_{py})) \\ \sigma_{py} &= \frac{E_p}{1 - \nu_p^2} (\epsilon_y - \epsilon_{py} + \nu(\epsilon_x - \epsilon_{px}))\end{aligned}\quad (5.3)$$

where E_p and ν_p are the Young's modulus and Poisson's ratio of the actuator respectively.

The longitudinal stresses inside the structure, σ_x and σ_y , also follow from Hooke's law:

$$\begin{aligned}\sigma_x &= \frac{E}{1 - \nu^2} (\epsilon_x + \nu\epsilon_y) \\ \sigma_y &= \frac{E}{1 - \nu^2} (\epsilon_y + \nu\epsilon_x).\end{aligned}\quad (5.4)$$

In pure flexural cases, the strain distribution across the plate thickness is linear, as shown in Figure 5.2, i.e. $\epsilon_x = \alpha_x z$ and $\epsilon_y = \alpha_y z$. Here, α_x and α_y are the strain gradients and z is the transverse distance from the neutral plane of the plate (see Figure 5.2). These strain gradients can be determined from the moment equilibrium equations below, assuming a perfect bonding between the piezoelectric patch and the plate:

$$\begin{aligned}\int_{-\frac{h}{2}}^{\frac{h}{2}} z \sigma_x dz + \int_{\frac{h}{2}}^{\frac{h}{2}+h_p} z \sigma_{px} dz &= 0 \\ \int_{-\frac{h}{2}}^{\frac{h}{2}} z \sigma_y dz + \int_{\frac{h}{2}}^{\frac{h}{2}+h_p} z \sigma_{py} dz &= 0.\end{aligned}\quad (5.5)$$

We substitute (5.3) and (5.4) into the moment equilibrium equations (5.5). The strain gradients are related to the free strains by

$$\begin{aligned}\alpha_x &= \kappa \epsilon_{px} \\ \alpha_y &= \kappa \epsilon_{py}\end{aligned}\quad (5.6)$$

where

$$\kappa = \frac{12 E_p h_p (h_p + h)}{24 D (1 - \nu_p^2) + E_p [(h + 2 h_p)^3 - h^3]}.\quad (5.7)$$

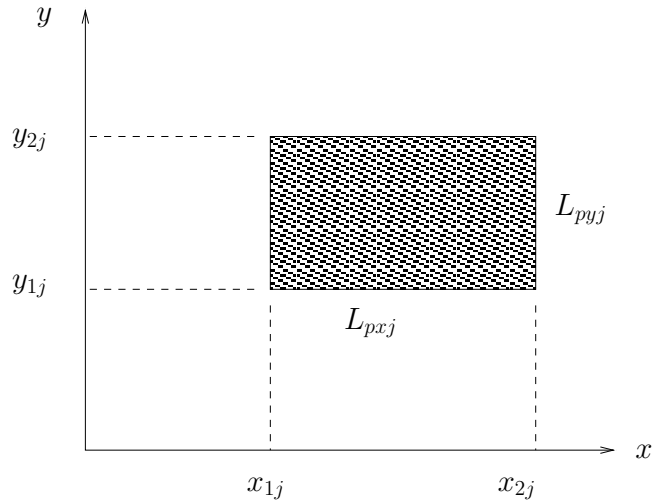


Figure 5.3: Coordinates of the j^{th} actuator patch

Suppose that the j^{th} actuator patch is located at (x_{1j}, y_{1j}) and (x_{2j}, y_{2j}) as shown in Figure 5.3. These two points correspond to the two opposite corner points of the patch since the patch is rectangular in shape. Here, we consider the case where $d_{31j} = d_{32j}$. The external moment per unit length generated by the j^{th} piezoelectric actuator can be obtained from the integrals in (5.5) using (5.6):

$$\begin{aligned}M_{pxj} &= M_{pyj} = \bar{A}_j [H(x - x_{1j}) - H(x - x_{2j})] \times \\ &\quad [H(y - y_{1j}) - H(y - y_{2j})] V_{aj}(t)\end{aligned}\quad (5.8)$$

where

$$\bar{A}_j = \frac{\kappa_j d_{31j} D(1 + \nu)}{h_{pj}} \quad (5.9)$$

and $H(\cdot)$ is a step function.

The external moment generated by the actuators $\partial^2 M_{pxj}/\partial x^2$ and $\partial^2 M_{pyj}/\partial y^2$ can be obtained by differentiating the M_{pxj} and M_{pyj} expressions twice with respect to x and y respectively. Hence, α_j in (5.1) can be shown to be:

$$\begin{aligned} \alpha_j = \bar{A}_j & \left\{ \left[\frac{d\delta(x - x_{1j})}{dx} - \frac{d\delta(x - x_{2j})}{dx} \right] \times \left[H(y - y_{1j}) - H(y - y_{2j}) \right] \right. \\ & \left. + \left[H(x - x_{1j}) - H(x - x_{2j}) \right] \times \left[\frac{d\delta(y - y_{1j})}{dy} - \frac{d\delta(y - y_{2j})}{dy} \right] \right\}. \end{aligned} \quad (5.10)$$

The PDE for flexural vibration of thin plates (2.37) is now solved using the modal analysis technique. The solution is in the form of

$$w(x, y, t) = \sum_{m=1}^{\infty} \sum_{n=1}^{\infty} \phi_{mn}(x, y) q_{mn}(t). \quad (5.11)$$

The eigenvalue problem is

$$D \nabla^4 \phi_{mn} = \rho h \omega_{mn}^2 \phi_{mn}. \quad (5.12)$$

As mentioned previously, ω_{mn} and ϕ_{mn} represent the natural frequency and eigenfunction associated with mode (m, n) respectively. Since D and ρh are constants, the eigenfunction ϕ_{mn} can be shown to have the following orthogonality properties:

$$\begin{aligned} \int_0^b \int_0^a \rho h \phi_{mn} \phi_{pq} dx dy &= \delta_{mp} \delta_{nq} \\ \int_0^b \int_0^a D \nabla^4 \phi_{mn} \phi_{pq} dx dy &= \omega_{mn}^2 \delta_{mp} \delta_{nq} \end{aligned} \quad (5.13)$$

where δ_{mp} and δ_{nq} are Kronecker delta functions.

Here, the contribution of external moments from all J actuators is considered. A set of ODE's obtained from modal analysis is

$$\omega_{mn}^2 q_{mn}(t) + 2\zeta_{mn} \omega_{mn} \dot{q}_{mn}(t) + \ddot{q}_{mn}(t) = \sum_{j=1}^J \int_0^b \int_0^a \phi_{mn}(x, y) \alpha_j dx dy V_{aj}(t) \quad (5.14)$$

where ζ_{mn} is the damping term that is introduced into the system.

In this case, we can assume that the eigenfunction consists of separate functions of x and y , such as in (2.65). Using the Dirac delta function property (2.78), the generalized force for piezoelectric actuators is

$$\sum_{j=1}^J \bar{A}_j \Psi_{mnj} V_{aj}(t)$$

where

$$\begin{aligned} \Psi_{mnj} = & \left[\int_{y_{1j}}^{y_{2j}} \frac{\partial \phi_{mn}(x_{2j}, y)}{\partial x} dy - \int_{y_{1j}}^{y_{2j}} \frac{\partial \phi_{mn}(x_{1j}, y)}{\partial x} dy \right] \\ & + \left[\int_{x_{1j}}^{x_{2j}} \frac{\partial \phi_{mn}(x, y_{2j})}{\partial y} dx - \int_{x_{1j}}^{x_{2j}} \frac{\partial \phi_{mn}(x, y_{1j})}{\partial y} dx \right]. \end{aligned} \quad (5.15)$$

Applying Laplace transform to (5.14) and assuming zero initial conditions, the transfer function from the actuator voltage $V_a(s) = [V_{a1}(s) \dots V_{aJ}(s)]^T$ to the plate deflection $w(s, x, y)$ is

$$G(s, x, y) = \sum_{m=1}^{\infty} \sum_{n=1}^{\infty} \frac{\phi_{mn}(x, y) P_{mn}}{\omega_{mn}^2 + 2\zeta_{mn} \omega_{mn} s + s^2} \quad (5.16)$$

where

$$P_{mn} = \left[\int_0^b \int_0^a \phi_{mn}(x, y) \alpha_1 dx dy \dots \int_0^b \int_0^a \phi_{mn}(x, y) \alpha_J dx dy \right]. \quad (5.17)$$

In particular, when piezoelectric actuators are used, then

$$P_{mn} = \left[\bar{A}_1 \Psi_{mn1} \dots \bar{A}_J \Psi_{mnJ} \right]. \quad (5.18)$$

5.1.1 Piezoelectric sensors

To observe vibrations of flexible structures, sensors are needed. Suppose there are J sensors distributed over the structure. A general description for the j^{th} sensor output is given by

$$v_j(t) = \sum_{m=1}^{\infty} \sum_{n=1}^{\infty} \left(C_{mnj} q_{mn}(t) + \bar{C}_{mnj} \dot{q}_{mn}(t) \right) \quad (5.19)$$

where C_{mnj} and \bar{C}_{mnj} depend on the properties and location of the sensor.

Consider the case when piezoelectric sensors are used [FEN96, LM90]. The j^{th} piezoelectric sensor is attached on the plate. We assume that all properties below belong to the sensor. The piezoelectric sensor is placed as shown in Figure 5.2. The electric charge inside the piezoelectric patch can be related to the strain:

$$q_p(t) = \frac{k_{31}^2}{g_{31}} \epsilon_x + \frac{k_{32}^2}{g_{32}} \epsilon_y \quad (5.20)$$

where k_{31} and k_{32} are the electromechanical coupling factors in x and y directions respectively. Also, g_{31} and g_{32} are the voltage constants in x and y directions. The contribution of the shear strain to the total electric charge is ignored since the axes of the sensor coincide with the geometrical axes of the plate, i.e. the sensor and the plate have similar orientation.

The strains, ϵ_x and ϵ_y , can be obtained from (2.24). In this case, z is the average distance from the neutral plane to the mid-plane of the sensor patch, i.e. $z = -(h + h_p)/2$. Hence,

$$\begin{aligned} \epsilon_x &= \frac{\partial u}{\partial x} = \frac{h + h_p}{2} \frac{\partial^2 w}{\partial x^2} \\ \epsilon_y &= \frac{\partial v}{\partial y} = \frac{h + h_p}{2} \frac{\partial^2 w}{\partial y^2}. \end{aligned} \quad (5.21)$$

Incorporating the strain expression in (5.21) into (5.20) and integrating the electric charge across the area of the sensor gives the induced voltage of the j^{th} sensor:

$$V_{sj}(t) = \frac{h + h_{pj}}{2C_j} \int_{y_{1j}}^{y_{2j}} \int_{x_{1j}}^{x_{2j}} \left[\frac{k_{31j}^2}{g_{31j}} \frac{\partial^2 w}{\partial x^2} + \frac{k_{32j}^2}{g_{32j}} \frac{\partial^2 w}{\partial y^2} \right] dx dy \quad (5.22)$$

where C_j is the piezoelectric capacitance.

After substituting the modal analysis solution (5.11), V_{sj} can be shown to be:

$$\begin{aligned} V_{sj}(t) &= \frac{h + h_{pj}}{2C_j} \sum_{m=1}^{\infty} \sum_{n=1}^{\infty} \left\{ \frac{k_{31j}^2}{g_{31j}} \left[\int_{y_{1j}}^{y_{2j}} \frac{\partial \phi_{mn}(x_{2j}, y)}{\partial x} dy \right. \right. \\ &\quad \left. \left. - \int_{y_{1j}}^{y_{2j}} \frac{\partial \phi_{mn}(x_{1j}, y)}{\partial x} dy \right] + \frac{k_{32j}^2}{g_{32j}} \left[\int_{x_{1j}}^{x_{2j}} \frac{\partial \phi_{mn}(x, y_{2j})}{\partial y} dx \right. \right. \\ &\quad \left. \left. - \int_{x_{1j}}^{x_{2j}} \frac{\partial \phi_{mn}(x, y_{1j})}{\partial y} dx \right] \right\} q_{mn}(t). \end{aligned} \quad (5.23)$$

The above expression shows how the placement of a piezoelectric sensor affect the sensitivity in sensing over a particular mode.

5.2 Optimal placement of actuators

This section discusses the optimization methodology for actuator placement of spatially distributed systems. The idea is to place actuators at locations where they provide desirable control authority, in a spatial sense, over the structure. For this purpose, we will define some relevant performance measures.

5.2.1 Spatial and modal controllability measures

Consider a thin plate with J actuators attached to it, whose transfer function is given in (5.16). G describes the dynamic response of the plate due to the excitation by J actuators.

The spatial \mathcal{H}_2 norm of G can be calculated by taking advantage of the orthogonality property of the eigenfunctions in (5.13) [MR99, MF98], following Theorem 3.2:

$$\begin{aligned} \ll G(s, x, y) \gg_2^2 &= \frac{1}{2\pi} \int_{-\infty}^{\infty} \int_0^b \int_0^a \operatorname{tr}\{G(j\omega, x, y)^* G(j\omega, x, y)\} dx dy d\omega \\ &= \sum_{m=1}^{\infty} \sum_{n=1}^{\infty} \|\tilde{G}_{mn}(s)\|_2^2 \end{aligned} \quad (5.24)$$

where

$$\tilde{G}_{mn} = \frac{P_{mn}}{\sqrt{\rho h}(s^2 + 2\zeta_{mn}\omega_{mn}s + \omega_{mn}^2)}. \quad (5.25)$$

Notice that \tilde{G}_{mn} , as described in (5.24), is the contribution of mode (m, n) to the spatial \mathcal{H}_2 norm of G . This property indicates how much control authority the actuators have over the structure for each mode. The level of control authority depends on the location at which the actuators are placed on the structure.

The above result is different from the additive property of modal norms proposed by Gawronski in [Gaw98]. The result in (5.24) arises from the spatial \mathcal{H}_2 norm definition for a spatial system which involves a spatial averaging on the spatial model. In contrast, the additive property in [Gaw98] is an approximation based on the fact that the coupling between modes is small for lightly damped

flexible structures, and is not based on a spatial averaging on the system. Interested readers should refer to [Gaw98] for details of the additive property.

Since $\|\tilde{G}_{mn}\|_2$ in (5.24) implies the level of authority of actuators over each mode, this measure can be used to determine the effectiveness of actuators to control each mode. Based on (5.24), we define a function

$$f_{mn}(x_1, y_1) = \|\tilde{G}_{mn}\|_2 \quad (5.26)$$

where f_{mn} depends on locations of actuators that are represented by (x_1, y_1) . The function can be normalized with respect to its maximum value to obtain the following:

Definition 5.1 Modal controllability: *The normalized value of f_{mn} in (5.26) is defined as the modal controllability of mode (m, n) [MR99]:*

$$\mathcal{M}_{mn}(x_1, y_1) = \frac{f_{mn}(x_1, y_1)}{\alpha_{mn}} \times 100\% \quad (5.27)$$

where $\alpha_{mn} = \max_{(x_1, y_1) \in \mathcal{R}_1} f_{mn}(x_1, y_1)$ and \mathcal{R}_1 is the set of all possible actuator locations.

The modal controllability indicates the authority of actuators over a specific mode. Naturally, if we wish to control a particular mode, the actuators should be placed at locations where the modal controllability of that mode is high.

Furthermore, the spatial \mathcal{H}_2 norm of the system in (5.24) indicates the control authority of the actuators over the entire structure in a spatially-averaged sense. Hence, the norm can be used as a measure of spatial controllability of a system. The spatial \mathcal{H}_2 norm of system G in (5.24) is contributed by f_{mn} associated with each mode. Here, the contribution of f_{mn} tends to be less for higher frequency modes since $\|1/(s^2 + 2\zeta_{mn}\omega_{mn}s + \omega_{mn}^2)\|_2$ decreases with ω_{mn} . This implies that it is reasonable to include only a few low frequency modes in the approximation of the spatial \mathcal{H}_2 norm.

Definition 5.2 Spatial controllability: *Suppose only the I_m lowest frequency modes are taken into account, the spatial controllability is [MR99]*

$$\mathcal{S}_c(x_1, y_1) = \frac{1}{\beta} \sqrt{\sum_{i=1}^{I_m} f_{m_i n_i}(x_1, y_1)^2} \times 100\% \quad (5.28)$$

where $\beta = \max_{(x_1, y_1) \in \mathcal{R}_1} \sqrt{\sum_{i=1}^{I_m} f_{m_i n_i}(x_1, y_1)^2}$. Here, m_i and n_i correspond to mode (m_i, n_i) , which is the i^{th} lowest frequency mode.

The spatial controllability is the normalized value of the approximate spatial \mathcal{H}_2 norm of the system, where β is the maximum value of the norm. The spatial controllability represents the actuator control authority contributed by selected modes. However, placing actuators in the location of highest spatial controllability may not be enough to ensure a good performance for every mode. It is possible that at the chosen locations, modal controllability of several modes may be unacceptably low. To avoid such a problem, a minimum level of modal controllability for each mode needs to be guaranteed. Hence, the actuators are to be placed in locations where the spatial controllability is sufficiently high. At the same time, the modal controllability of each important mode has to be above a certain minimum level.

5.2.2 Control spillover reduction

Here, we extend the optimization methodology to take into account the control spillover effect. Suppose that the actuators are optimally placed according to the previous procedure. It is still possible that the chosen locations correspond to high modal controllability for higher frequency modes. This leads to a control spillover problem which may affect the performance of the controller since the actuators could be exciting the higher frequency modes.

It is thus important to place restrictions on the authority of several high-frequency modes. This can be done by restricting the level of modal controllability of those modes, which will add extra constraints to the optimization [HM02b]. An alternative is to add only one extra constraint that guarantees a

sufficiently low level of spatial controllability for several higher frequency modes. By doing so, the spillover effect on the system can be reduced. Suppose a few higher frequency modes from mode $I_m + 1$ up to mode \bar{I} are considered. Several higher frequency modes can be chosen, and the spatial controllability associated with these modes is expressed in the following:

Definition 5.3 Spatial controllability for spillover:

$$\mathcal{S}_{c2}(x_1, y_1) = \frac{1}{\beta_2} \sqrt{\sum_{i=I_m+1}^{\bar{I}} f_{m_i n_i}(x_1, y_1)^2} \times 100\% \quad (5.29)$$

where $\beta_2 = \max_{(x_1, y_1) \in \mathcal{R}_1} \sqrt{\sum_{i=I_m+1}^{\bar{I}} f_{m_i n_i}(x_1, y_1)^2}$ and \bar{I} corresponds to the highest frequency mode that is considered for the control spillover reduction.

Therefore, the constrained optimization problem for optimal placement of actuators can be set up as:

$$\begin{aligned} & \max_{(x_1, y_1) \in \mathcal{R}_1} \mathcal{S}_c(x_1, y_1) \\ & \text{subject to: } \mathcal{M}_{m_i n_i}(x_1, y_1) \geq b_i, \quad i = 1, 2, \dots, I_m \\ & \mathcal{S}_{c2}(x_1, y_1) \leq c \end{aligned} \quad (5.30)$$

where (m_i, n_i) is the mode corresponding to the i^{th} lowest frequency mode, and b_i is the minimum level for modal controllability of mode (m_i, n_i) . Also, c is the highest allowable level for spatial controllability for spillover reduction.

We can set the allowable levels for modal controllability and spatial controllability depending on the requirements. For reduction of control spillover, it is important to include only a few dominant higher frequency modes. It is not practical to include too many constraints in the optimization. It may be sufficient to consider only a few such modes since the controller can be designed so that its response will roll off at higher frequencies. Thus, the spillover effect can be reduced even further.

An extension to this optimal placement methodology is to include only a number of selected modes that are of control significance, and not all low frequency modes. In this case, the spatial controllability \mathcal{S}_c is calculated based on

only the selected modes, while \mathcal{S}_{c2} is calculated based on several other modes that are important for spillover reduction purposes.

5.3 Optimal placement of sensors

In this section, we propose a new optimal placement methodology for sensors. Here, we introduce a performance measure that can be used to indicate the authority of sensors over the entire structure in a spatially-averaged sense.

5.3.1 Spatial and modal observability measures

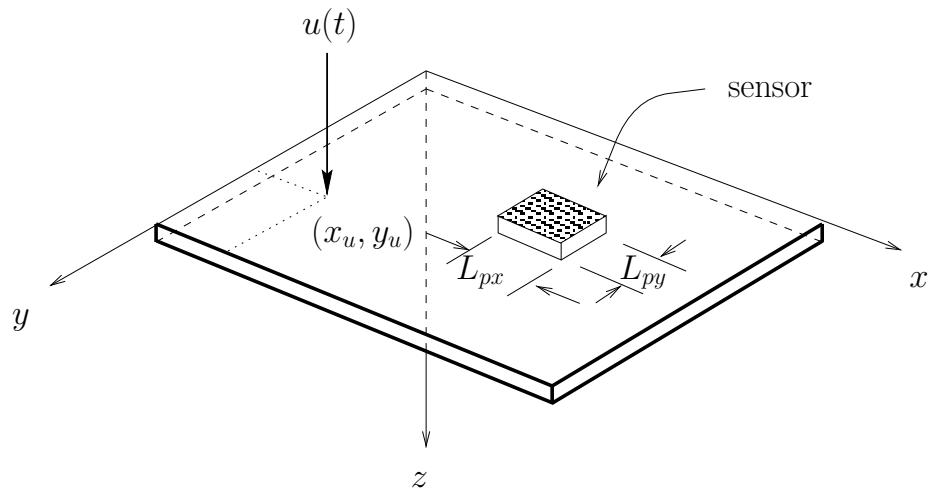


Figure 5.4: A plate with a piezoelectric sensor and a point disturbance $u(t)$

Consider a point disturbance u acting on a structure at an arbitrarily chosen location (x_u, y_u) as shown in Figure 5.4. This disturbance causes structural vibration that may be observed by sensors. The generalized force as in (2.49) can be found to be:

$$\int_0^b \int_0^a \phi_{mn}(x, y) \delta(x - x_u) \delta(y - y_u) dx dy u(t) = \phi_{mn}(x_u, y_u) u(t). \quad (5.31)$$

Suppose there are J sensors distributed over the structure. The j^{th} sensor observes the structural vibration according to (5.19). The transfer function from

the point disturbance u to the sensor output $v = [v_1 \dots v_J]^T$ is

$$G_{vu}(s, x_u, y_u) = \sum_{m=1}^{\infty} \sum_{n=1}^{\infty} \frac{\phi_{mn}(x_u, y_u) (Q_{mn} + \bar{Q}_{mn}s)}{s^2 + 2\zeta_{mn}\omega_{mn}s + \omega_{mn}^2} \quad (5.32)$$

where

$$\begin{aligned} Q_{mn} &= [C_{mn1} \dots C_{mnJ}]^T \\ \bar{Q}_{mn} &= [\bar{C}_{mn1} \dots \bar{C}_{mnJ}]^T. \end{aligned} \quad (5.33)$$

Notice that the transfer function G_{vu} depends on where the disturbance is acting on a structure, i.e. it is a function of the spatial location (x_u, y_u) .

Suppose we wish to find the best place for the sensors, assuming that the disturbance comes from that specific location at (x_u, y_u) . We may consider the placement that optimizes the energy of the sensor signal due to the excitation of the point disturbance. We may use a measure of the output energy due to a white noise input signal that is represented by the \mathcal{H}_2 norm of the system G_{vu} . This allows the sensor to be located at a location where it can observe effectively the structural vibration caused by a point disturbance at (x_u, y_u) . However, the sensor may not be able to effectively observe vibration caused by disturbances at other locations.

To ensure that vibration caused by disturbances at other locations can be observed in a spatial sense, it is advantageous to include the spatial information contained in the system. As a consequence, we use a measure that can incorporate the spatial information of the system, which is the spatial \mathcal{H}_2 norm. We will need the following theorem:

Theorem 5.1 Consider $G_{vu}(s, x_u, y_u)$ in (5.32), then

$$\ll G_{vu} \gg_2^2 = \sum_{m=1}^{\infty} \sum_{n=1}^{\infty} \bar{f}_{mn}^2 \quad (5.34)$$

where

$$\bar{f}_{mn}(x_1, y_1) = \sqrt{\frac{1}{\rho h} \sum_{j=1}^J \left\| \frac{C_{mnj} + \bar{C}_{mnj}s}{s^2 + 2\zeta_{mn}\omega_{mn}s + \omega_{mn}^2} \right\|_2^2} \quad (5.35)$$

and \bar{f}_{mn} is a function of the sensor locations that are expressed by (x_1, y_1) .

Proof

$$\begin{aligned}
\ll G_{vu}(s, x_u, y_u) \gg_2^2 &= \frac{1}{2\pi} \int_{-\infty}^{\infty} \int_0^b \int_0^a \{G_{vu}(j\omega, x_u, y_u)^* G_{vu}(j\omega, x_u, y_u)\} dx_u dy_u d\omega \\
&= \frac{1}{2\pi} \int_{-\infty}^{\infty} \int_0^b \int_0^a \left\{ \sum_{m=1}^{\infty} \sum_{n=1}^{\infty} \frac{\phi_{mn}(x_u, y_u)(Q_{mn}^T - \bar{Q}_{mn}^T j\omega)}{(\omega_{mn}^2 - \omega^2) - 2\zeta_{mn}\omega_{mn}j\omega} \right. \\
&\quad \left. \times \sum_{p=1}^{\infty} \sum_{q=1}^{\infty} \frac{\phi_{pq}(x_u, y_u)(Q_{pq} + \bar{Q}_{pq}j\omega)}{(\omega_{pq}^2 - \omega^2) + 2\zeta_{pq}\omega_{pq}j\omega} \right\} dx_u dy_u d\omega
\end{aligned}$$

Incorporating the orthogonality condition of the eigenfunctions (5.13) and since Q_{mn} and \bar{Q}_{mn} are described in (5.33), we have

$$\begin{aligned}
\ll G_{vu} \gg_2^2 &= \frac{1}{\rho h} \times \frac{1}{2\pi} \int_{-\infty}^{\infty} \sum_{m=1}^{\infty} \sum_{n=1}^{\infty} \sum_{j=1}^J \frac{C_{mnj} - \bar{C}_{mnj}j\omega}{(\omega_{mn}^2 - \omega^2) - 2\zeta_{mn}\omega_{mn}j\omega} \\
&\quad \times \frac{C_{mnj} + \bar{C}_{mnj}j\omega}{(\omega_{mn}^2 - \omega^2) + 2\zeta_{mn}\omega_{mn}j\omega} d\omega \\
&= \frac{1}{\rho h} \sum_{m=1}^{\infty} \sum_{n=1}^{\infty} \sum_{j=1}^J \left\| \frac{C_{mnj} + \bar{C}_{mnj}s}{s^2 + 2\zeta_{mn}\omega_{mn}s + \omega_{mn}^2} \right\|_2^2.
\end{aligned}$$

Note that G_{vu} is a column vector, so no trace operation is required to compute the norm. This completes the proof.

The measure used in Theorem 5.1 differs from the one used for actuator placement since now the input signal is spatially distributed over the structure. On the other hand, for actuator placement, the output signal is spatially distributed. The theorem shows that the spatial \mathcal{H}_2 norm of G_{vu} contains an independent contribution from each mode. It is interesting to compare this with the spatial \mathcal{H}_2 norm of G in (5.24). Both results show the contribution of each mode to the spatial \mathcal{H}_2 norm of certain systems without any mode coupling. The result of this theorem simplifies the optimization for sensor placement significantly since the contribution of each mode is clearly defined.

In a physical sense, the system spatial \mathcal{H}_2 norm measures the detected signal energy of the sensor due to excitation of a point disturbance at all possible locations over the structure in a spatially-averaged sense. Since the system is

linear and arbitrary disturbances can be regarded as a linear superposition of point disturbances, the measure also reflects the way sensors will perform when the structure is excited by arbitrary disturbances. Hence, we can optimize the placement of sensors by finding locations where the value of the spatial \mathcal{H}_2 norm is sufficiently high. Based on Theorem 5.1, we can define several measures as follows:

Definition 5.4 Modal observability: *The modal observability of mode (m, n) is a normalized value of \bar{f}_{mn} in (5.35):*

$$\mathcal{K}_{mn}(x_1, y_1) = \frac{\bar{f}_{mn}(x_1, y_1)}{\bar{\alpha}_{mn}} \times 100\% \quad (5.36)$$

where $\bar{\alpha}_{mn} = \max_{(x_1, y_1) \in \mathcal{R}_1} \bar{f}_{mn}(x_1, y_1)$.

The modal observability of mode (m, n) represents the level of contribution of the mode to the spatial \mathcal{H}_2 norm of the system G_{vu} .

Definition 5.5 Spatial observability: *Suppose that only the I_m lowest frequency modes are of interest. The spatial observability is a normalized value of the approximate $\ll G_{vu} \gg_2$ in (5.34):*

$$\mathcal{S}_o(x_1, y_1) = \frac{1}{\bar{\beta}} \sqrt{\sum_{i=1}^{I_m} \bar{f}_{m_i n_i}(x_1, y_1)^2} \times 100\% \quad (5.37)$$

where $\bar{\beta} = \max_{(x_1, y_1) \in \mathcal{R}_1} \sqrt{\sum_{i=1}^{I_m} \bar{f}_{m_i n_i}(x_1, y_1)^2}$. Here, m_i and n_i correspond to mode (m_i, n_i) , which is the i^{th} lowest frequency mode.

5.3.2 Observation spillover reduction

The sensors that are placed on the structure may have high authority in observing some high frequency modes that are not of control significance. This leads to the observation spillover that may be detrimental to the closed-loop performance and stability. We can define the spatial observability for several higher frequency modes to reduce the effect of observation spillover.

Definition 5.6 Spatial observability for spillover reduction: *The spatial observability for spillover reduction \mathcal{S}_{o2} is defined as:*

$$\mathcal{S}_{o2}(x_1, y_1) = \frac{1}{\bar{\beta}_2} \sqrt{\sum_{i=I_m+1}^{\bar{I}} \bar{f}_{m_i n_i}(x_1, y_1)^2} \times 100\% \quad (5.38)$$

where $\bar{\beta}_2 = \max_{(x_1, y_1) \in \mathcal{R}_1} \sqrt{\sum_{i=I_m+1}^{\bar{I}} \bar{f}_{m_i n_i}(x_1, y_1)^2}$ and \bar{I} corresponds to the highest frequency mode that is considered for the observation spillover reduction.

Therefore, the optimization problem for optimal placement of sensors is

$$\begin{aligned} & \max_{(x_1, y_1) \in \mathcal{R}_1} \mathcal{S}_o(x_1, y_1) \\ & \text{subject to: } \mathcal{K}_{m_i n_i}(x_1, y_1) \geq b_i, \quad i = 1, 2, \dots, I_m \\ & \mathcal{S}_{o2}(x_1, y_1) \leq c \end{aligned} \quad (5.39)$$

where b_i is the minimum level for modal observability of mode (m_i, n_i) , while c is the highest allowable level for spatial observability for spillover reduction.

As in the case for actuator placement, it is also possible to include only a number of selected modes in determining \mathcal{S}_o and \mathcal{S}_{o2} . Therefore, we can concentrate on only selected modes that are of control significance.

5.4 Optimal placement of piezoelectric actuators and sensors

In this section, we implement the results based on the previous sections for a specific case of piezoelectric actuators and sensors. It has been shown that the moment generated by rectangular piezoelectric actuators depends on locations of the corner points of the patches. Similarly, the amount of voltage induced by piezoelectric sensors also depends on locations of the corner points. This fact makes the placement of the actuators and sensors interesting. It is important to be able to place these actuators and sensors at locations where they have sufficiently high authority over those modes that are of control significance.

The previous results in optimal placement methodology allow the placement for several actuators and sensors simultaneously. However, simultaneous placement may complicate the optimization when actuators/sensors have considerable dimensions relative to the structure, such as for the case of piezoelectric actuators/sensors. The difficulty is due to the fact that geometric constraints have to be included to prevent patches overlapping. Hence, our approach here is to consider the optimal placement for each piezoelectric actuator/sensor. The geometric constraints can then be considered by selecting possible locations that do not overlap patches. It is obvious that some compromises are needed.

As mentioned previously, we assume negligible contribution of piezoelectric patches to the overall mass and stiffness of the structure. This assumption is useful in simplifying the optimization, since initially the locations of patches are unknown. This assumption is reasonable as the patches that are commonly used are relatively thin with respect to the thickness of the main structure. However, when the dimensions of patches are considerable, the contributions of the patches to the structure may be significant. Hence, an iterative optimization process will be needed because the overall structural properties will be a function of the actuator/sensor location.

5.4.1 Piezoelectric actuators

Consider the placement of a single actuator, say the j^{th} actuator. In this case, we consider only a single input version of system G in (5.16), i.e. the transfer function from j^{th} actuator signal to the structural deflection. Each modal contribution depends on the location of the j^{th} actuator on the structure. Thus, if we intend to find the optimal placement for the actuator, the contribution of mode (m, n) due to the j^{th} actuator is $\|\tilde{G}_{mnj}\|_2^2$, where

$$\tilde{G}_{mnj} = \frac{P_{mnj}}{\sqrt{\rho h}(s^2 + 2\zeta_{mn}\omega_{mn}s + \omega_{mn}^2)} \quad (5.40)$$

and $P_{mnj} = \bar{A}_j \Psi_{mnj}$ is described in (5.18). Suppose that one corner of the j^{th} piezoelectric actuator patch with a fixed size is located at x_{1j} and y_{1j} , as shown

in Figure 5.3. A function f_{mnj} can be defined as:

$$\begin{aligned} f_{mnj}(x_{1j}, y_{1j}) &= \|\tilde{G}_{mnj}\|_2 \\ &= \left\| \frac{\bar{A}_j \Psi_{mnj}(x_{1j}, y_{1j})}{\sqrt{\rho h}} \right\| \left\| \frac{1}{s^2 + 2\zeta_{mn}s + \omega_{mn}^2} \right\|_2 \end{aligned} \quad (5.41)$$

The modal controllability is

$$\mathcal{M}_{mn}(x_{1j}, y_{1j}) = \frac{f_{mnj}(x_{1j}, y_{1j})}{\alpha_{mnj}} \times 100\% \quad (5.42)$$

where $\alpha_{mnj} = \max_{(x_{1j}, y_{1j}) \in \mathcal{R}_1} f_{mnj}(x_{1j}, y_{1j})$ and \mathcal{R}_1 is the set of all possible actuator locations.

If only the I_m lowest frequency modes are taken into account, the spatial controllability is

$$\mathcal{S}_c(x_{1j}, y_{1j}) = \frac{1}{\beta_j} \sqrt{\sum_{i=1}^{I_m} f_{m_i n_i j}(x_{1j}, y_{1j})^2} \times 100\% \quad (5.43)$$

where $\beta_j = \max_{(x_{1j}, y_{1j}) \in \mathcal{R}_1} \sqrt{\sum_{i=1}^{I_m} f_{m_i n_i j}(x_{1j}, y_{1j})^2}$.

Several higher frequency modes can be chosen to reduce control spillover and the spatial controllability contributed by these modes \mathcal{S}_{c2} is

$$\mathcal{S}_{c2}(x_{1j}, y_{1j}) = \frac{1}{\beta_{2j}} \sqrt{\sum_{i=I_m+1}^{\bar{I}} f_{m_i n_i j}(x_{1j}, y_{1j})^2} \times 100\% \quad (5.44)$$

where $\beta_{2j} = \max_{(x_{1j}, y_{1j}) \in \mathcal{R}_1} \sqrt{\sum_{i=I_m+1}^{\bar{I}} f_{m_i n_i j}(x_{1j}, y_{1j})^2}$ and \bar{I} again corresponds to the highest frequency mode that is considered for the control spillover reduction. Hence, the optimization problem for the placement of piezoelectric actuators can be set up as in (5.30).

5.4.2 Piezoelectric sensors

For the case where $k_{31} = k_{32}$ and $g_{31} = g_{32}$, the voltage induced in the j^{th} piezoelectric sensor $V_{sj}(t)$ in (5.23) can be shown to be:

$$V_{sj}(t) = \frac{k_{31j}^2}{C_j g_{31j}} \left(\frac{h + h_{pj}}{2} \right) \sum_{m=1}^{\infty} \sum_{n=1}^{\infty} \Psi_{mnj}(x_{1j}, y_{1j}) q_{mn}(t) \quad (5.45)$$

where Ψ_{mnj} is in (5.15).

If we compare V_{sj} to the general description for the j^{th} sensor output v_j (5.19), we can observe that

$$V_{sj}(t) = \sum_{m=1}^{\infty} \sum_{n=1}^{\infty} C_{mnj} q_{mn}(t) \quad (5.46)$$

where C_{mnj} is obtained from (5.45). Then from Theorem 5.1, we obtain \bar{f}_{mn} for the j^{th} sensor:

$$\bar{f}_{mnj}(x_1, y_1) = \sqrt{\frac{1}{\rho h} \left\| \frac{C_{mnj}}{s^2 + 2\zeta_{mn}\omega_{mn}s + \omega_{mn}^2} \right\|_2^2}. \quad (5.47)$$

Hence, the modal observability can be defined as:

$$\mathcal{K}_{mn}(x_{1j}, y_{1j}) = \frac{\bar{f}_{mnj}(x_{1j}, y_{1j})}{\bar{\alpha}_{mnj}} \times 100\% \quad (5.48)$$

where

$$\begin{aligned} \bar{f}_{mnj} &= \left| \frac{k_{31j}^2}{C_j g_{31j} \sqrt{\rho h}} \left(\frac{h + h_{pj}}{2} \right) \Psi_{mnj}(x_{1j}, y_{1j}) \right| \left\| \frac{1}{s^2 + 2\zeta_{mn}\omega_{mn}s + \omega_{mn}^2} \right\|_2 \\ \bar{\alpha}_{mnj} &= \max_{(x_{1j}, y_{1j}) \in \mathcal{R}_1} \bar{f}_{mnj}(x_{1j}, y_{1j}). \end{aligned} \quad (5.49)$$

The spatial observability is

$$\mathcal{S}_o(x_{1j}, y_{1j}) = \frac{1}{\bar{\beta}_j} \sqrt{\sum_{i=1}^{I_m} \bar{f}_{m_i n_i j}(x_{1j}, y_{1j})^2} \times 100\% \quad (5.50)$$

where $\bar{\beta}_j = \max_{(x_{1j}, y_{1j}) \in \mathcal{R}_1} \sqrt{\sum_{i=1}^{I_m} \bar{f}_{m_i n_i j}(x_{1j}, y_{1j})^2}$.

Moreover, the spatial observability for observation spillover reduction is

$$\mathcal{S}_{o2}(x_{1j}, y_{1j}) = \frac{1}{\bar{\beta}_{2j}} \sqrt{\sum_{i=I_m+1}^{\bar{I}} \bar{f}_{m_i n_i j}(x_{1j}, y_{1j})^2} \times 100\% \quad (5.51)$$

where $\bar{\beta}_{2j} = \max_{(x_{1j}, y_{1j}) \in \mathcal{R}_1} \sqrt{\sum_{i=I_m+1}^{\bar{I}} \bar{f}_{m_i n_i j}(x_{1j}, y_{1j})^2}$.

The optimization problem for the placement of piezoelectric sensors is similar to that of the general case in (5.39).

Now, consider a particular case where identical piezoelectric patches are used as actuators and sensors. By comparison of (5.42) and (5.48), \mathcal{M} and \mathcal{K} are

clearly similar since they are both linearly proportional to $|\Psi_{mnj}(x_{1j}, y_{1j})|$, which is the only function that depends on the locations of patches. Hence, the spatial controllability and spatial observability are also similar. That is

$$\begin{aligned}\mathcal{M}_{mn}(x_{1j}, y_{1j}) &= \mathcal{K}_{mn}(x_{1j}, y_{1j}) \\ \mathcal{S}_c(x_{1j}, y_{1j}) &= \mathcal{S}_o(x_{1j}, y_{1j}) \\ \mathcal{S}_{c2}(x_{1j}, y_{1j}) &= \mathcal{S}_{o2}(x_{1j}, y_{1j}).\end{aligned}\tag{5.52}$$

The above results have an implication on the optimal placement of a collocated piezoelectric actuator/sensor pair. Suppose we place a piezoelectric actuator on a structure that gives certain levels of spatial controllability and modal controllability. Placing a piezoelectric sensor at the same location would yield similar levels of spatial observability and modal observability. Thus, we only need to optimize the placement of either actuator or sensor.

A similar optimization procedure can be used to find the optimal position and size of each collocated actuator/sensor pair to obtain optimal spatial controllability, while maintaining sufficient modal controllability levels. In this case, four optimization variables are needed, two variables for the position, and the other two for the actuator/sensor size.

5.5 Illustrative example: a plate structure

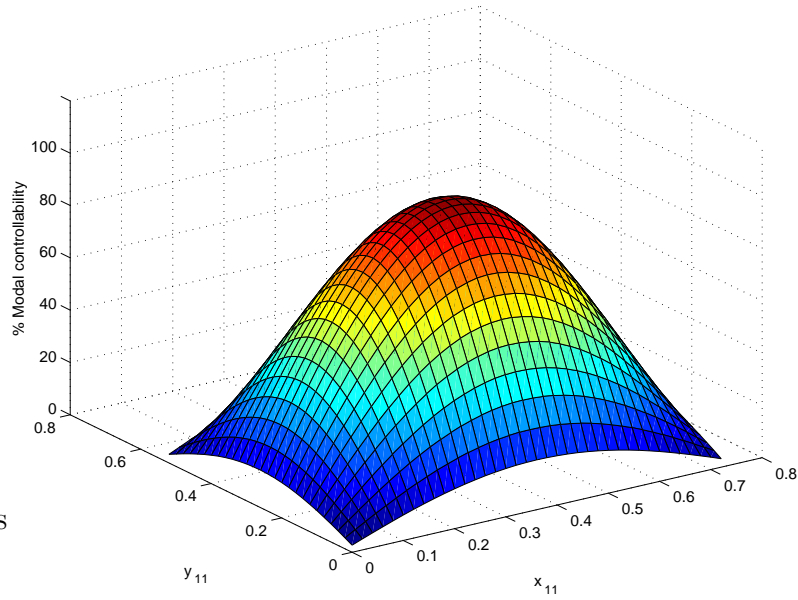
We consider the optimal placement of a collocated piezoelectric actuator/sensor pair on a thin rectangular plate with simply-supported edges. The piezoelectric actuator/sensor pair has similar properties in x and y directions, i.e. $k_{31} = k_{32}$, $g_{31} = g_{32}$ and $d_{31} = d_{32}$. The sizes of the patches are fixed and they are oriented in similar directions with respect to the plate. The properties of the plate and piezoelectric patches used are similar to those used in Chapter 4 (see Table 4.1). Initially, each mode of the plate is assumed to have a damping ratio of $\zeta_{mn} = 0.002$. This, however, is later refined using the experimental data obtained from the experimental rig.

No.	Mode (m, n)	Frequency (Hz)
1	(1, 1)	41.9
2	(2, 1)	87.1
3	(1, 2)	122.4
4	(3, 1)	162.4
5	(2, 2)	167.6
6	(3, 2)	242.9
7	(1, 3)	256.5
8	(4, 1)	267.9
9	(2, 3)	301.7
10	(4, 2)	348.3

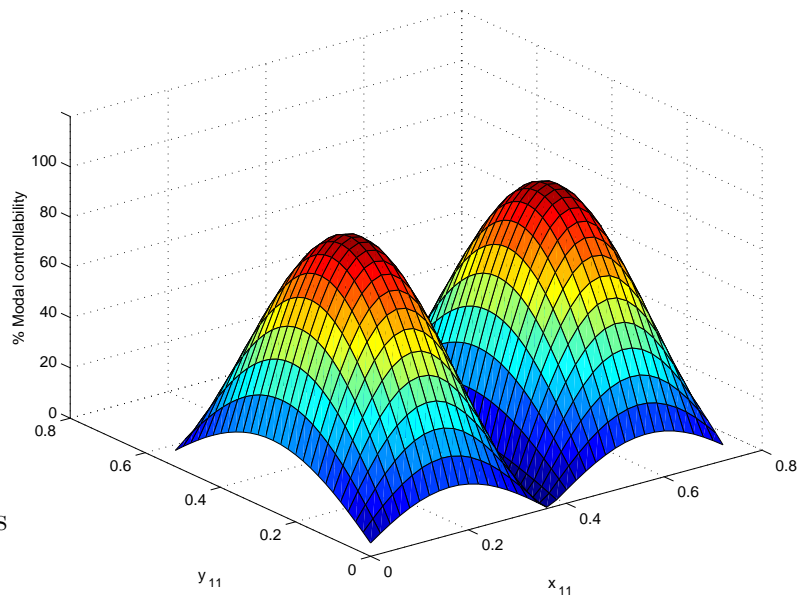
Table 5.1: First ten modes of the plate

Following the previous result, we only need to optimize the placement of the piezoelectric actuator. The previous optimization procedure is employed for this purpose. In this case, we wish to maximize \mathcal{S}_c that is contributed by the first five modes. For control spillover reduction, the next five modes are considered. Table 5.1 shows the frequencies of the relevant modes obtained from the simulated model.

Figures 5.5, 5.6 and 5.7 show the modal controllability of the first five modes versus the piezoelectric actuator location. The location of the patch is described as the location of one corner of the patch (x_{11}, y_{11}). For example, it is observed that the maximum modal controllability of 100% for mode (1, 1) occurs when one of the corners of the actuator is placed at $x_{11} = 0.36$ m and $y_{11} = 0.26$ m. This location corresponds to placing the actuator in the middle of the plate.

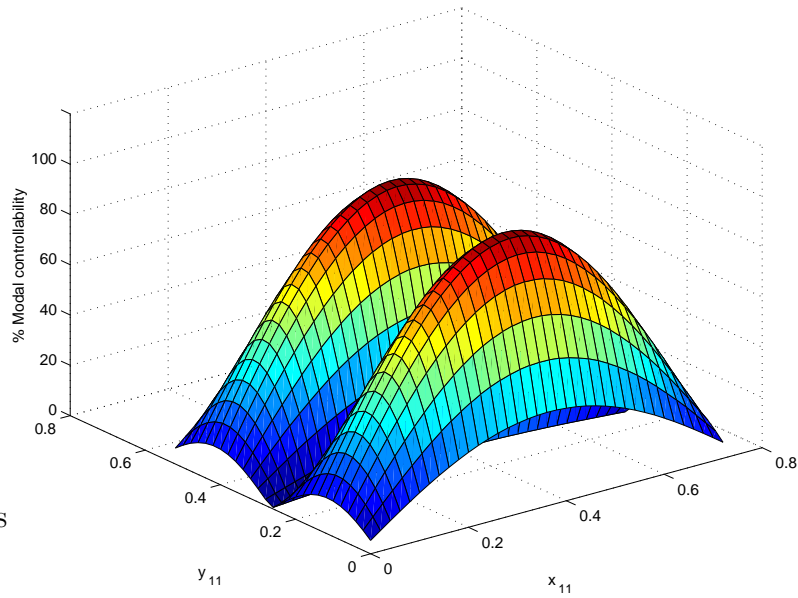


(a) mode (1,1)

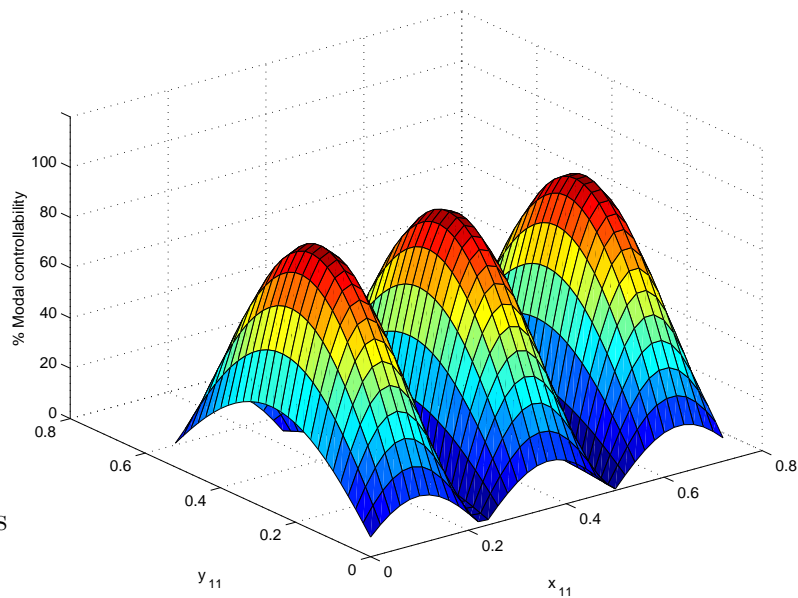


(b) mode (2,1)

Figure 5.5: Modal controllability - modes 1 and 2

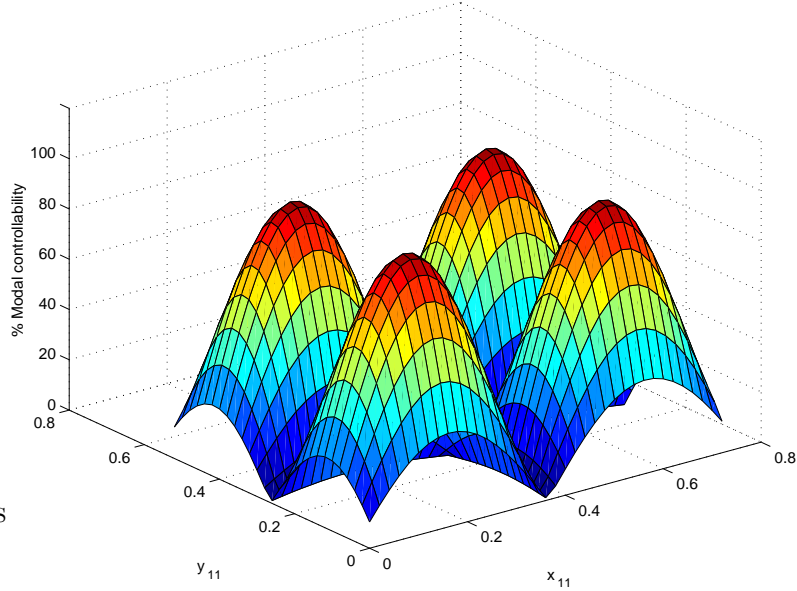


(a) mode (1,2)



(b) mode (3,1)

Figure 5.6: Modal controllability - modes 3 and 4



(a) mode (2,2)

Figure 5.7: Modal controllability - mode 5

Figure 5.8 shows the spatial controllability \mathcal{S}_c due to the first five modes. If an actuator is placed in the middle of the plate, it would have a considerably high spatial controllability. Figure 5.9 shows the spatial controllability for the next five modes for control spillover reduction \mathcal{S}_{c2} . It is desirable to find a location where \mathcal{S}_{c2} is sufficiently small.

We set the minimum level of modal controllability for the first five modes at 50% for each mode. The contributions to spatial \mathcal{H}_2 norm of the next five modes are limited to 60%. The constrained optimization problem is set up as follows:

$$\begin{aligned}
 & \max_{(x_{11}, y_{11}) \in \mathcal{R}_1} \mathcal{S}_c(x_{11}, y_{11}) \\
 & \text{subject to: } \mathcal{M}_{m_i n_i}(x_{11}, y_{11}) \geq 50\%, \quad i = 1, 2, \dots, 5 \\
 & \mathcal{S}_{c2}(x_{11}, y_{11}) \leq 60\%.
 \end{aligned} \tag{5.53}$$

The optimization problem is then solved using the Matlab Optimization Toolbox. The optimum solution found is $x_{11} = 0.1536$ m and $y_{11} = 0.1418$ m, where

$$\begin{aligned}
 \mathcal{S}_c &= 92.6\% \\
 \mathcal{M}_{11} &= 55.1\% \\
 \mathcal{M}_{21} &= 80.6\% \\
 \mathcal{M}_{12} &= 65.3\% \\
 \mathcal{M}_{31} &= 63.4\% \\
 \mathcal{M}_{22} &= 96.1\% \\
 \mathcal{S}_{c2} &= 55.6\%.
 \end{aligned} \tag{5.54}$$

This solution shows that the optimal spatial controllability is over 90%, while maintaining the modal controllability of all five modes above 50%. On the other hand, the spatial controllability \mathcal{S}_{c2} of the next five higher frequency modes is also maintained at a level below 60%, which means that the contributions of those modes to the control spillover will be relatively low. In general, the objective function \mathcal{S}_c has multiple local optima. A range of initial guesses for x_{11} and y_{11} have been tried to obtain the global optimum. The optimization result shows that the collocated piezoelectric actuator/sensor pair should be placed at $x_{11} = 0.1536$ m and $y_{11} = 0.1418$ m as also shown in Figure 4.1.

5.5.1 Experiments

Here, we will validate the results that we obtain from the previous optimization on a plate structure. The plate was made from an aluminium alloy, which was held by a supporting frame. At design stage, FE modelling using STRAND7 software was performed to ensure sufficient rigidity of the supporting frame up to at least 350 Hz, which would cover the first ten vibration modes based on our plate model. The supporting frame is shown in Figure 5.10. The plate and frame apparatus were placed on an optical table to minimize external vibrations affecting the experimental measurements (see Figure 5.11). We used aluminium shims to simulate the simply-supported boundary condi-

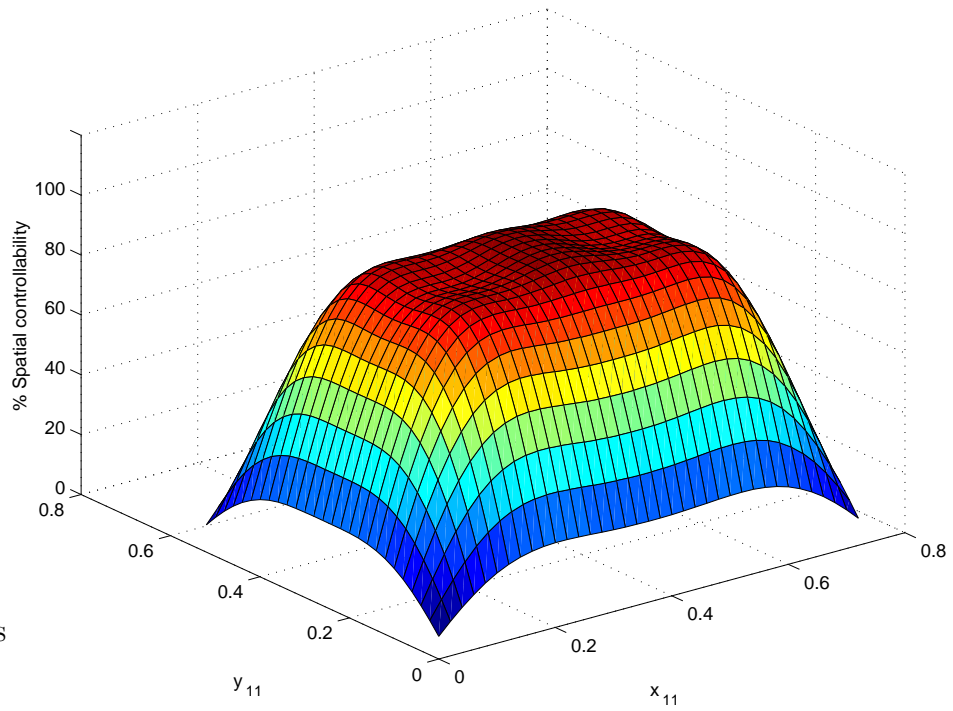
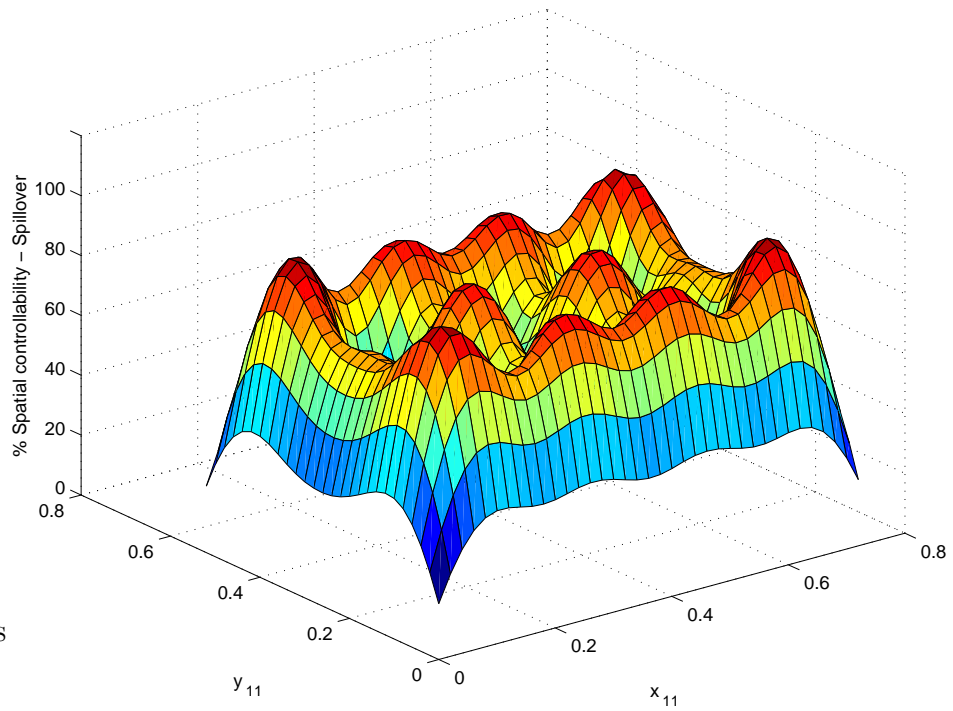
Figure 5.8: Spatial controllability \mathcal{S}_c - based on the first five modesFigure 5.9: Spatial controllability \mathcal{S}_{c2} (control spillover reduction)



Figure 5.10: The supporting frame

tions as shown in Figure 5.12. The shims were inserted along the edges of the plate and clamped to the supporting frame. Based on our observation, the shims approximated simply-supported boundary conditions sufficiently, although some degree of rotational and transverse movements of the shims were expected.

A high voltage amplifier, capable of driving highly capacitive loads, was used to supply necessary voltage for the piezoelectric actuator. An HP89410A Dynamic Signal Analyzer and a Polytec PSV-300 Laser Doppler Scanning Vibrometer were used to obtain frequency responses from the piezoelectric laminate plate.

Table 5.2 compares the experimentally measured, and the simulated six lowest resonance frequencies of the plate. Larger errors were observed at higher frequencies. The errors of the model in predicting the actual resonance frequencies vary around a few percent. In general, the model is reasonably close to the actual plate based on our experimental results.

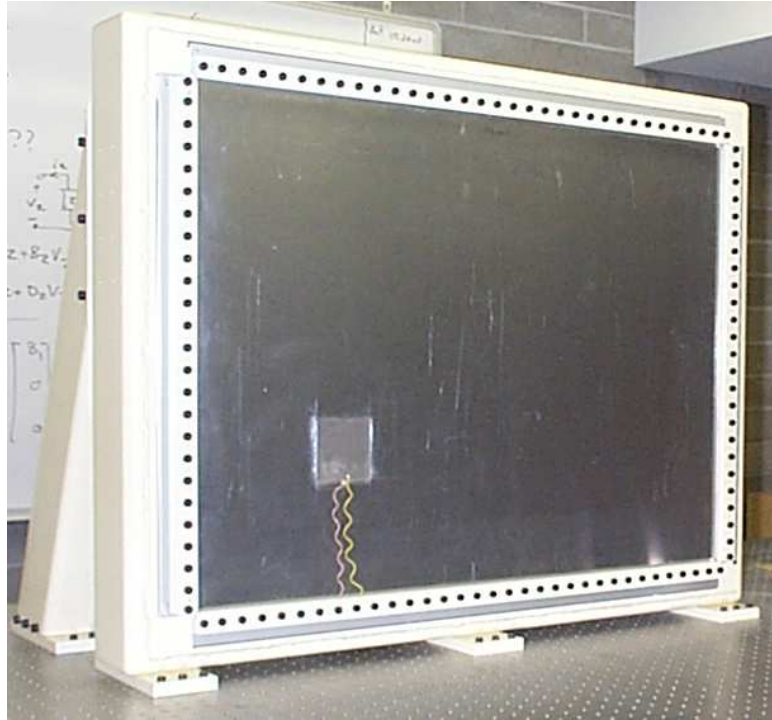


Figure 5.11: The experimental apparatus

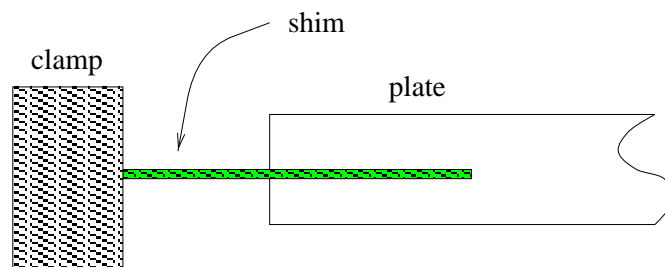
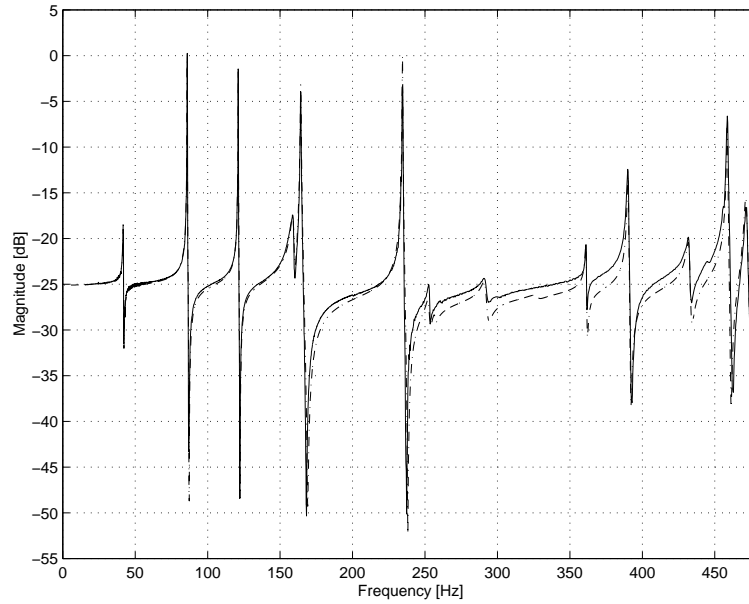
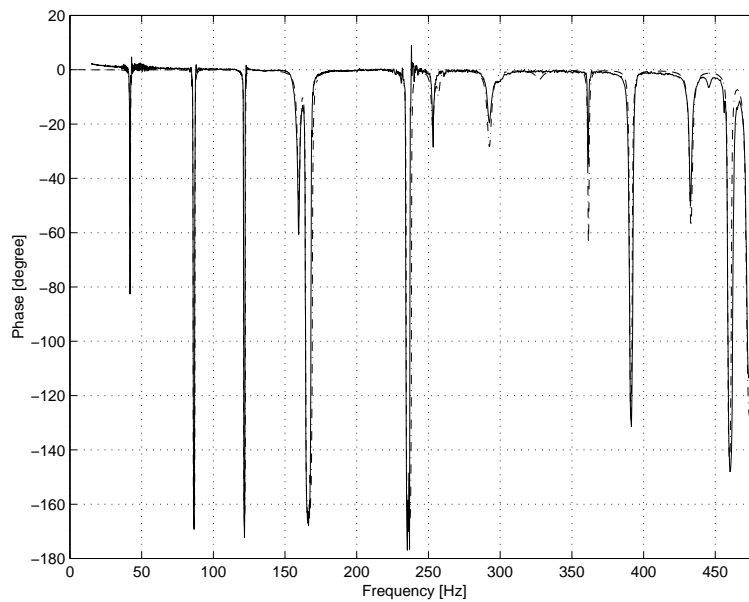


Figure 5.12: Shims - boundary conditions



(a) magnitude



(b) phase

Figure 5.13: The frequency response of the collocated actuator/sensor system: a plate structure [V/V]

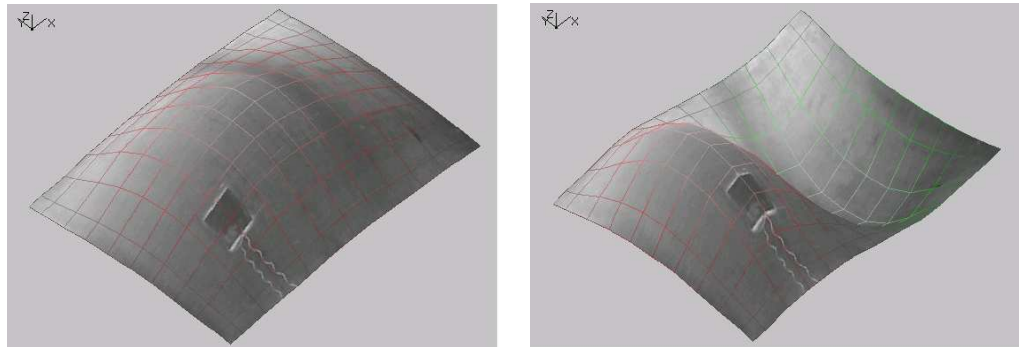
No.	Mode (m, n)	Simulation ω_{mn} (Hz)	Experiment ω_{mn} (Hz)	Error (%)
1	(1, 1)	41.9	41.8	0.2
2	(2, 1)	87.1	85.9	1.4
3	(1, 2)	122.4	121.1	1.1
4	(3, 1)	162.4	159.2	2.0
5	(2, 2)	167.6	164.3	2.0
6	(3, 2)	242.9	234.5	3.6

Table 5.2: First six modes of the plate

Figure 5.13 compares frequency responses of the collocated actuator/sensor system. The dashed line represents the simulation, while the solid line represents the experimental results. The resonance frequencies and damping ratios from the experiment have been used to correct the model. The experimental results show reasonably close response between the simulation and experiment.

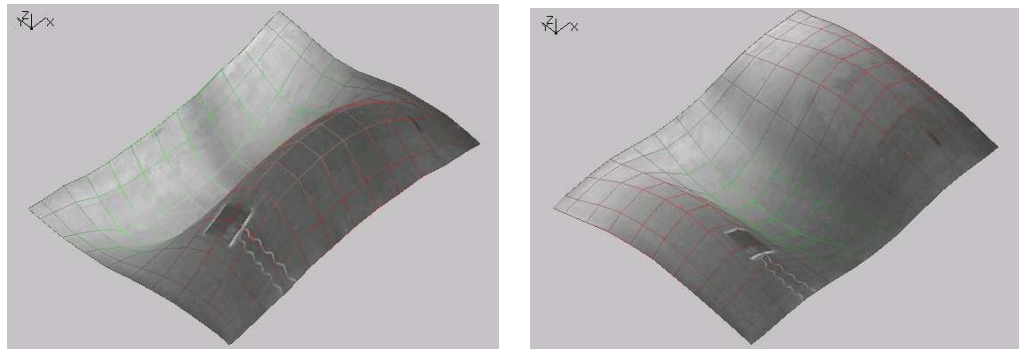
It is observed that the first five modes from 41.8 Hz to 164.3 Hz, have relatively large resonant responses. Furthermore, in the optimization, the spatial controllability/observability contribution of the next five modes from 234.5 Hz to 327.2 Hz has been reduced to 55.6% to reduce the spillover effect. The result can be observed in Figure 5.13 where the next five modes, but not the sixth mode (at 234.5 Hz), have less resonant responses than the first five modes. It is noticed that mode 8 at 256.9 Hz and mode 10 at 327.2 Hz can hardly be seen in the figure.

The sixth mode at 234.5 Hz has a comparable profile to those of the first five modes. This is not surprising since the optimization process only reduces the spatial controllability level associated with modes 6 to 10. We can also try to reduce the modal controllability level corresponding to each of those modes



(a) mode (1, 1)

(b) mode (2, 1)



(c) mode (1, 2)

(d) mode (3, 1)

Figure 5.14: Mode shapes of the first four modes

to ensure that each modal controllability is sufficiently low. However, more constraints will result in a more complex optimization problem.

Figure 5.14 shows the mode shapes that were obtained using the PSV-300 Laser Doppler Scanning Vibrometer. The mode shapes are reasonably close to the mode shapes for a simply-supported plate in Figure 2.13. It confirms our prediction that the use of aluminium shims for the simply-supported boundary conditions is reasonable, at least for low frequency modes.

5.6 Optimal placement for finite element based models

The optimal placement of a collocated piezoelectric actuator/sensor pair on a simply-supported plate has been discussed previously. The notions of spatial controllability/observability and modal controllability/observability have been found to be useful for dealing with the optimal placement problem. These performance measures can be used for finding the optimal placement of actuators/sensors for models that are based from modal analysis [MR99, HM99].

However, many complex structures cannot be modelled using the modal analysis method. Alternative modelling methods such as the FE method can be useful for modelling such structures. Thus, it is convenient to extend the previous developed methodology for more general structures, which can be modelled using approximate methods. This section is aimed at extending the previous methodology to FE based models. In particular, we concentrate on the FE model of a beam described in Section 2.7.

Consider a flexible beam, with several actuators attached to it, whose transfer function is described in (2.111):

$$G_r(s, r) = \sum_{i=1}^k \frac{C_w(r) \phi_i P_i}{s^2 + 2\zeta_i \omega_i s + \omega_i^2}$$

where $r \in \mathcal{R} = \{r \mid 0 \leq r \leq L\}$ and $P_i = \phi_i^T \bar{F}$. The transfer function only includes a finite number of modes k that are obtained from the FE formulation. Since higher frequency modes obtained from the FE method are less accurate than the lower frequency modes, it is necessary to include only the lower frequency modes for the modelling. To obtain a relatively accurate model with k modes, Meirovitch [Mei75] suggests constructing a FE model of at least $2k$ modes.

For general structures, Theorem 3.2 cannot be used to calculate the spatial \mathcal{H}_2 norm of G_r since the orthogonality property in (3.6) is not satisfied. However, Lemma 4.2 states that the eigenvectors are orthogonal with respect to the

distributed mass. Therefore, we propose to use the weighted spatial \mathcal{H}_2 norm as a performance measure (see Definition 3.4). Based on Theorem 4.1, we use the following performance measure as the spatial controllability measure:

$$\ll G_r(s, r) \gg_{2,m}^2 = \sum_{i=1}^k f_i^2 \quad (5.55)$$

where

$$f_i(r_1) = \left\| \frac{P_i}{s^2 + 2\zeta_i\omega_i s + \omega_i^2} \right\|_2. \quad (5.56)$$

Here, we assume that the locations of actuators are represented by $r_1 \in \mathcal{R}_1$ where \mathcal{R}_1 is the set of all possible locations of actuators.

From (5.55) and (5.56), we can define the spatial controllability \mathcal{S}_c and modal controllability \mathcal{M}_i in the following:

Definition 5.7 Spatial controllability: *Suppose only the first I_m modes are of interest, then the spatial controllability is*

$$\mathcal{S}_c(r_1) = \frac{1}{\beta} \sqrt{\sum_{i=1}^{I_m} f_i(r_1)^2} \times 100\% \quad (5.57)$$

where $\beta = \max_{r_1 \in \mathcal{R}_1} \sqrt{\sum_{i=1}^{I_m} f_i(r_1)^2}$.

Definition 5.8 Modal controllability: *The modal controllability is*

$$\mathcal{M}_i(r_1) = \frac{f_i(r_1)}{\alpha_i} \times 100\% \quad (5.58)$$

where $\alpha_i = \max_{r_1 \in \mathcal{R}_1} f_i(r_1)$.

Furthermore, we can also consider the optimal placement of sensors for FE based models. As in Section 5.3, we consider a transfer function that relates a point disturbance u at location r_u to the signals observed by sensors. The nodal forces can be calculated by calculating the virtual work done by the structure:

$$\begin{aligned} \delta \bar{W}(t) &= \int_0^L \delta(r - r_u) u(t) \delta w(t, r) dr \\ &= \delta w(t, r_u) u(t). \end{aligned} \quad (5.59)$$

Since displacement w can be expressed as in (2.96), we obtain

$$\begin{aligned}\delta\bar{W}(t) &= C_w(r_u)\delta w(t)u(t) \\ &= \hat{F}(t)^T\delta w(t).\end{aligned}\quad (5.60)$$

Thus, the nodal force is $\hat{F} = C_w(r_u)^T u(t)$ where $u(t)$ is a scalar.

We consider a general j^{th} sensor whose output can be described by

$$v_j(t) = \sum_{i=1}^k \left(C_{ij}^v q_i(t) + \bar{C}_{ij}^v \dot{q}_i(t) \right) \quad (5.61)$$

where C_{ij}^v and \bar{C}_{ij}^v are constants that depend on the properties and location of the sensor.

If there are J sensors distributed over the structure, then the transfer function from the point disturbance to sensor output $v = [v_1 \dots v_J]^T$ is

$$G_{vu}(s, r_u) = \sum_{i=1}^k \frac{(Q_i + \bar{Q}_i s) \phi_i^T C_w(r_u)^T}{s^2 + 2\zeta_i \omega_i s + \omega_i^2} \quad (5.62)$$

where

$$\begin{aligned}Q_i &= [C_{i1}^v \dots C_{iJ}^v]^T \\ \bar{Q}_i &= [\bar{C}_{i1}^v \dots \bar{C}_{iJ}^v]^T.\end{aligned}\quad (5.63)$$

Again, the weighted spatial \mathcal{H}_2 norm is used as a performance measure of the sensors. The distributed mass m is used as the spatial weighting function. The following theorem is central for the optimal placement of sensors:

Theorem 5.2 Consider the transfer function G_{vu} in (5.62), then

$$\ll G_{vu}(s, r_u) \gg_{2,m}^2 = \sum_{i=1}^k \bar{f}_i^2 \quad (5.64)$$

where

$$\bar{f}_i = \sqrt{\sum_{j=1}^J \left\| \frac{C_{ij}^v + \bar{C}_{ij}^v s}{s^2 + 2\zeta_i \omega_i s + \omega_i^2} \right\|_2^2}. \quad (5.65)$$

Proof We use the fact that for two compatible column vectors, x and y , then $x^T y = \text{tr} \{xy^T\}$. Since G_{vu} is also a column vector, we have

$$\begin{aligned}
\ll G_{vu} \gg_{2,m}^2 &= \frac{1}{2\pi} \int_{-\infty}^{\infty} \int_0^L \{G_{vu}(j\omega, r_u)^* m(r_u) G_{vu}(j\omega, r_u)\} dr_u d\omega \\
&= \frac{1}{2\pi} \int_{-\infty}^{\infty} \int_0^L \text{tr} \{G_{vu}(-j\omega, r_u) m(r_u) G_{vu}(j\omega, r_u)^T\} dr_u d\omega \\
&= \frac{1}{2\pi} \int_{-\infty}^{\infty} \int_0^L \text{tr} \left\{ \sum_{i=1}^k \frac{(Q_i - \bar{Q}_i j\omega) \phi_i^T C_w(r_u)^T}{(\omega_i^2 - \omega^2) - 2\zeta_i \omega_i j\omega} \times m(r_u) \right. \\
&\quad \left. \times \sum_{l=1}^k \frac{C_w(r_u) \phi_l (Q_l^T + \bar{Q}_l^T j\omega)}{(\omega_l^2 - \omega^2) + 2\zeta_l \omega_l j\omega} \right\} dr_u d\omega \\
&= \frac{1}{2\pi} \int_{-\infty}^{\infty} \text{tr} \left\{ \sum_{i=1}^k \frac{(Q_i - \bar{Q}_i j\omega)}{(\omega_i^2 - \omega^2) - 2\zeta_i \omega_i j\omega} \times \frac{(Q_i^T + \bar{Q}_i^T j\omega)}{(\omega_i^2 - \omega^2) + 2\zeta_i \omega_i j\omega} \right\} d\omega
\end{aligned}$$

where the last equation is obtained by incorporating the orthogonality condition in Lemma 4.2. Since Q_i and \bar{Q}_i are defined as in (5.63), we can further simplify the equation to obtain:

$$\ll G_{vu} \gg_{2,m}^2 = \sum_{i=1}^k \sum_{j=1}^J \left\| \frac{C_{ij}^v + \bar{C}_{ij}^v s}{s^2 + 2\zeta_i \omega_i s + \omega_i^2} \right\|_2^2.$$

This completes the proof.

Based on Theorem 5.2, we can define the following performance measures:

Definition 5.9 Modal observability: The modal observability can be obtained from (5.65), where

$$\mathcal{K}_i(r_1) = \frac{\bar{f}_i(r_1)}{\bar{\alpha}_i} \times 100\% \quad (5.66)$$

where $\bar{\alpha}_i = \max_{r_1 \in \mathcal{R}_1} \bar{f}_i(r_1)$.

The spatial observability can now be set up using the result in (5.64).

Definition 5.10 Spatial observability: If only the I_m lowest frequency modes are taken into account, the spatial observability is defined as:

$$\mathcal{S}_o(r_1) = \frac{1}{\bar{\beta}} \sqrt{\sum_{i=1}^{I_m} \bar{f}_i(r_1)^2} \times 100\% \quad (5.67)$$

where $\bar{\beta} = \max_{(r_1) \in \mathcal{R}_1} \sqrt{\sum_{i=1}^{I_m} \bar{f}_i(r_1)^2}$.

Hence, optimization problems similar to those in (5.30) and (5.39) can also be set up for FE based models.

5.7 Illustrative example: a wing model

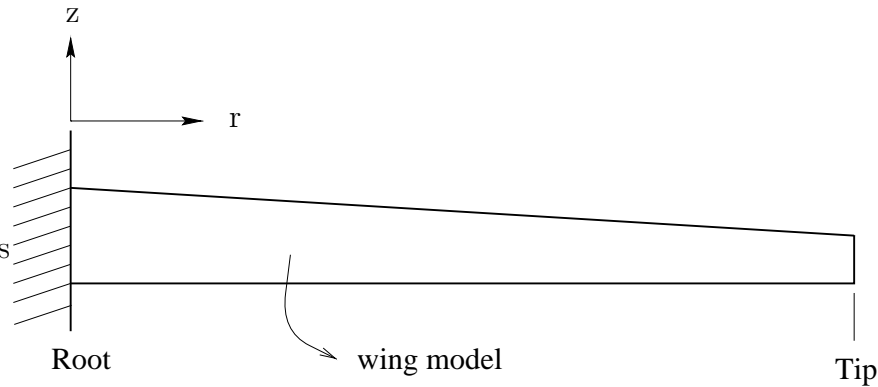


Figure 5.15: A wing model

We consider the optimal placement of a piezoelectric actuator patch over a wing model to illustrate our optimization methodology for FE models. The wing model is shown in Figure 5.15. The wing is modelled by a flexible beam with a uniform thickness h . The moment of inertia I and the cross-sectional area A of the wing linearly change across the half wing span as shown in Figure 5.16. Table 5.3 gives some of the properties of the wing model. A damping ratio of 0.002 for the wing model is assumed for each mode. The size of the patch is fixed, so we only need to optimize the location of one end of the patch.

We wish to find the actuator placement that gives relatively high control authority over the first four modes. On the other hand, we also wish to reduce the authority of the next three modes. The model consists of 20 modes, which is sufficient since only the first seven modes are of interest.

The optimization procedure given earlier in (5.30) is used. In this case the four lowest frequency modes are used to calculate the spatial controllability level \mathcal{S}_c . The next three higher frequency modes are considered for control spillover reduction. Table 5.4 shows the frequencies of the relevant modes.

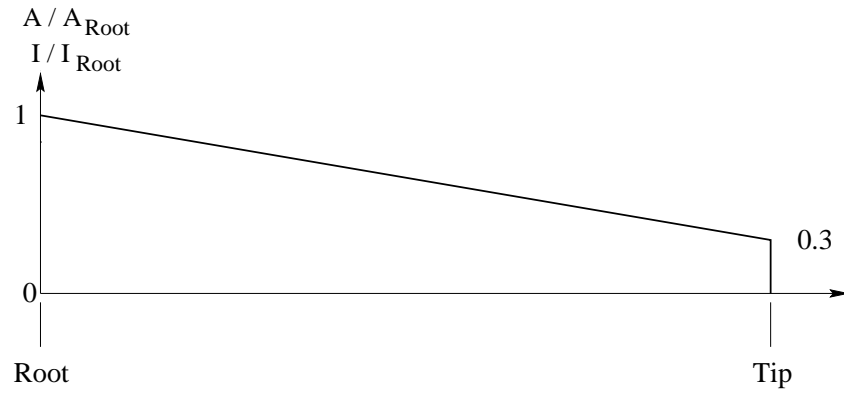


Figure 5.16: The wing property distribution

Half wing span, L	6.0 m
Wing thickness, h	0.10 m
Wing Young's modulus, E	7.50×10^{10} N/m ²
Wing root moment of inertia, I_{root}	3.50×10^{-6} m ⁴
Wing root cross-sectional area, A_{root}	4.00×10^{-3} m ²
Wing density, ρ_b	2.77×10^3 kg/m ³
Piezoceramic r -length	0.30 m
Piezoceramic z -length	0.15 m
Piezoceramic thickness	2.00×10^{-3} m
Piezoceramic Young's modulus, E_p	6.60×10^{10} N/m ²
Charge constant, d_{31}	-1.90×10^{-10} m/V
Voltage constant, g_{31}	-1.16×10^{-2} Vm/N
Capacitance, C	4.00×10^{-8} F
Electromechanical coupling factor, k_{31}	0.32

Table 5.3: Properties of the wing model

Mode	Frequency (Hertz)
1	3.35
2	16.8
3	43.9
4	84.2
5	137.9
6	205.1
7	285.7

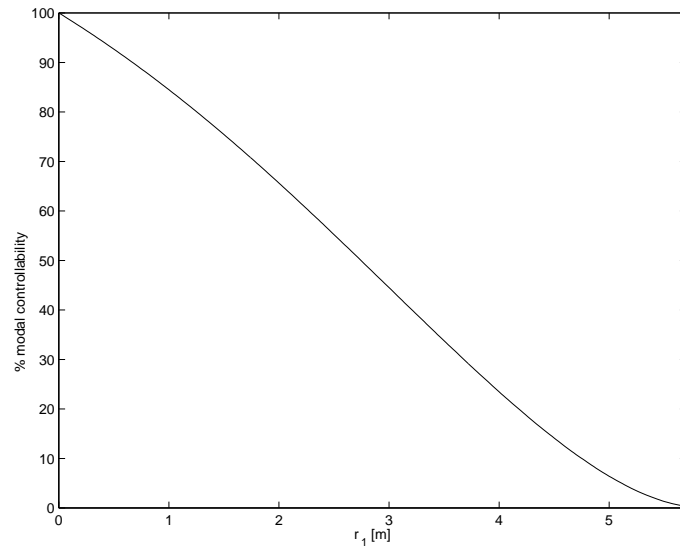
Table 5.4: First seven modes of the wing model

Figures 5.17 and 5.18 show the modal controllability of the first four modes of the plate versus the piezoelectric actuator location on the plate. For example, it can be observed that the maximum modal controllability of 100% for mode 2 happens when one end of the actuator patch is placed at $r_1 = 3.3$ m. The spatial controllability is plotted in Figure 5.19. It can be observed that an actuator placed in the region near the wing root has a considerably high spatial controllability level. Figures 5.20 and 5.21 show the modal controllability of the next three modes for control spillover reduction.

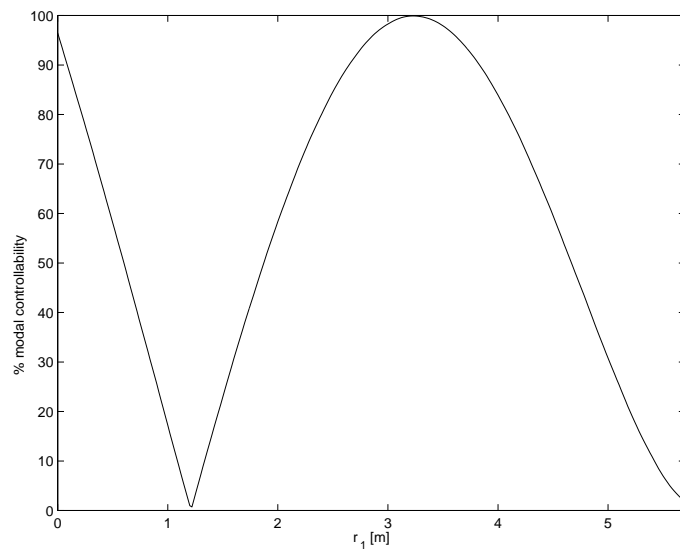
The constrained optimization problem is set up as:

$$\begin{aligned} & \max_{r_1 \in \mathcal{R}_1} \mathcal{S}_c(r_1) \\ & \text{subject to: } \mathcal{M}_i(r_1) \geq 50\%, \quad i = 1, \dots, 4 \\ & \quad \quad \quad \mathcal{M}_i(r_1) \leq 50\%, \quad i = 5, \dots, 7 \end{aligned}$$

The minimum level of modal controllability for each of the first four modes is thus set at 50% for each mode, while the modal controllability level for each of the next three modes is limited to 50%. The optimization problem is then

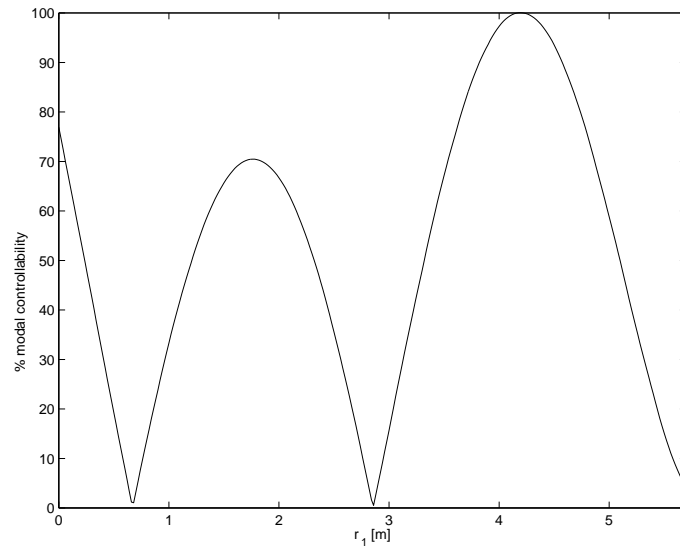


(a) mode 1

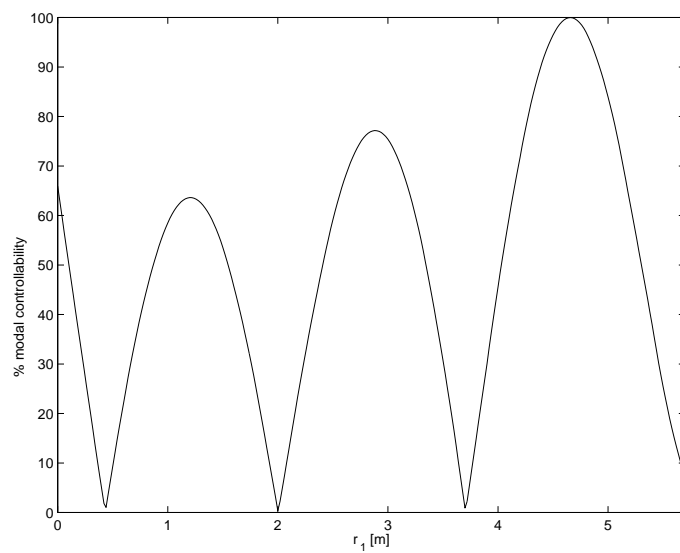


(b) mode 2

Figure 5.17: Modal controllability - modes 1 and 2



(a) mode 3



(b) mode 4

Figure 5.18: Modal controllability - modes 3 and 4

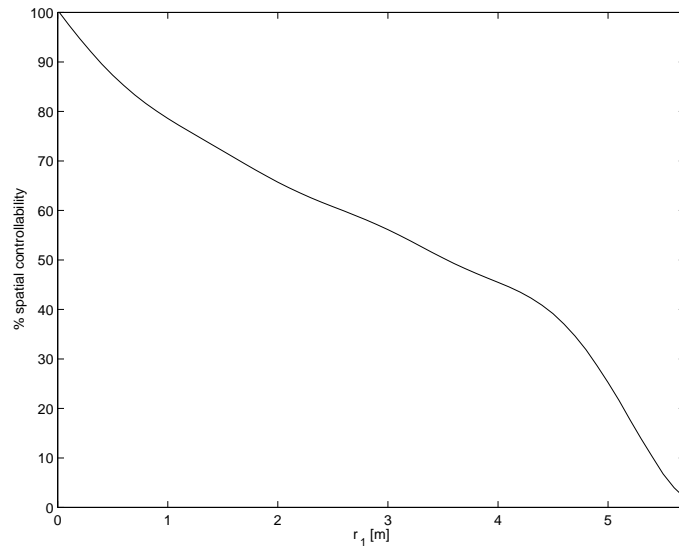


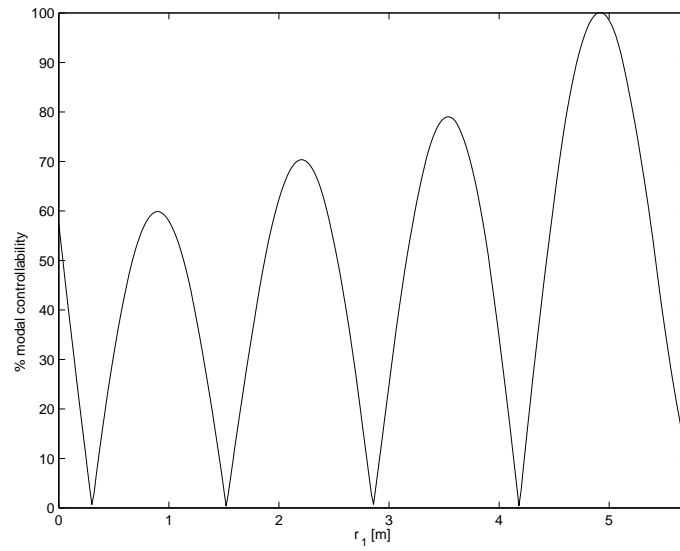
Figure 5.19: Spatial controllability - based on the first four modes

solved using the Matlab Optimization Toolbox. A range of initial guesses for r_1 needs to be tried to obtain a satisfying solution or the global optimum. The optimum solution is obtained at $r_1 = 0.0370$ m with

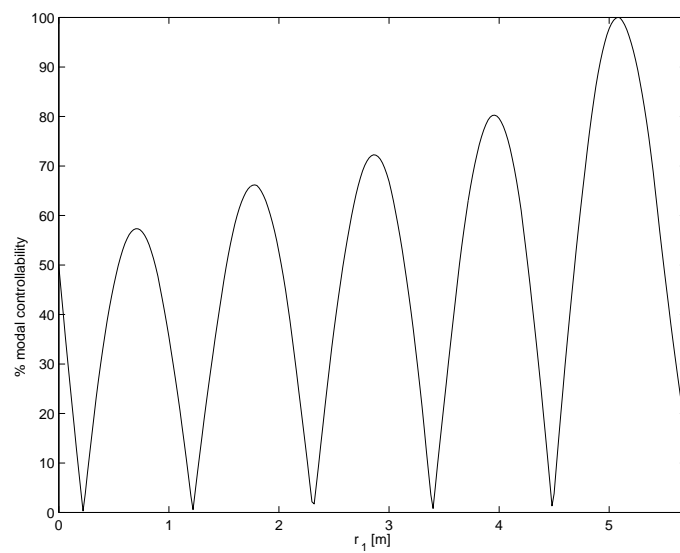
$$\begin{aligned}
 \mathcal{S}_c &= 99.7\% \\
 \mathcal{M}_1 &= 99.5\% \\
 \mathcal{M}_2 &= 93.7\% \\
 \mathcal{M}_3 &= 72.7\% \\
 \mathcal{M}_4 &= 60.1\% \\
 \mathcal{M}_5 &= 50.0\% \\
 \mathcal{M}_6 &= 40.9\% \\
 \mathcal{M}_7 &= 32.7\%
 \end{aligned}$$

The result corresponds to placing the actuator close to the root. This is as expected because of high average strain at the root of a cantilevered structure.

As mentioned in Section 5.4.2, the controllability and observability levels are similar for a system with an identical collocated piezoelectric actuator/sensor pair. Hence, it is reasonable to analyze the optimization results from the collo-

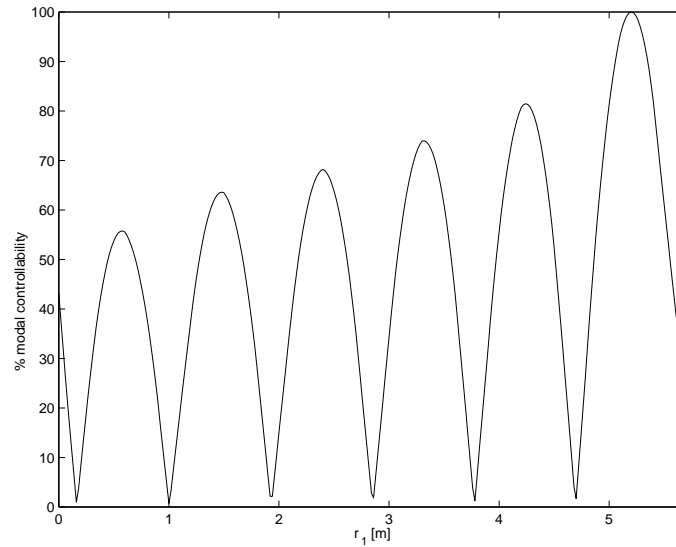


(a) mode 5



(b) mode 6

Figure 5.20: Modal controllability - modes 5 and 6



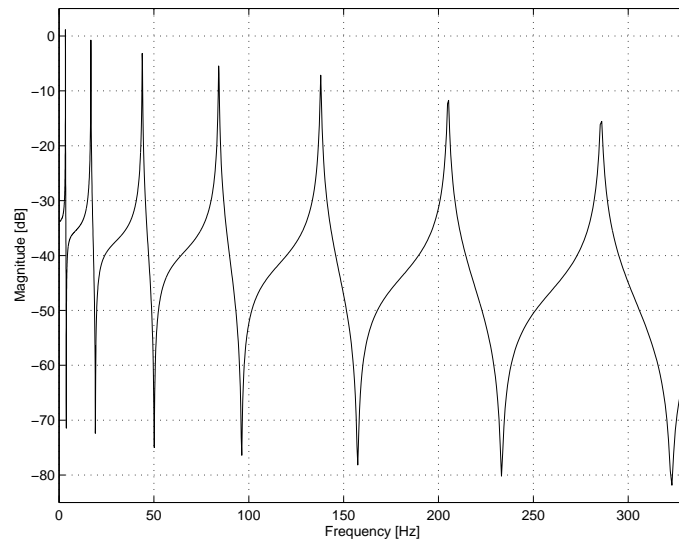
(a) mode 7

Figure 5.21: Modal controllability - mode 7

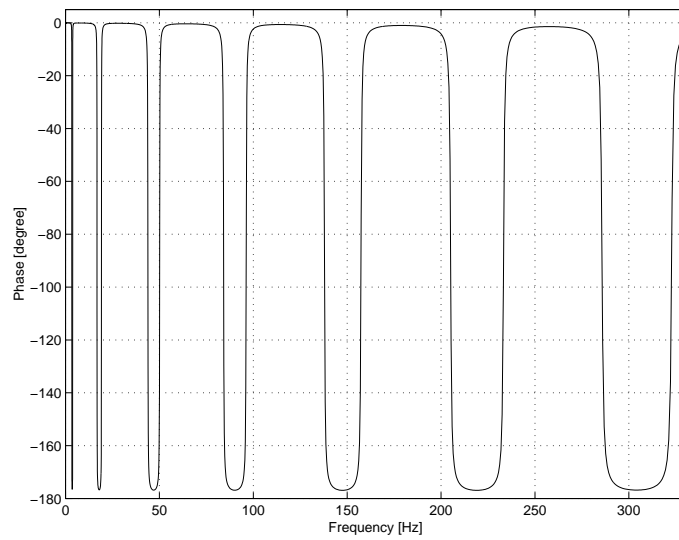
cated actuator/sensor frequency response in Figure 5.22. The first four modes show higher resonant responses than the next three modes. This reflects the modal controllability level of each mode obtained previously.

5.8 Optimal placement for other modelling methods

As mentioned in Section 4.5, the estimated eigenfunctions from other approximate methods (such as Rayleigh-Ritz and assumed-modes methods) are orthogonal with respect to the distributed mass [Mei75]. Hence, using the approximate weighted spatial \mathcal{H}_2 norm of the system as the spatial controllability/observability measure, we can derive the optimal placement methodology in a similar way.



(a) magnitude



(b) phase

Figure 5.22: The frequency response of the collocated actuator/sensor system: a wing model [V/V]

For models that are obtained from system identification, a similar result can be obtained. For instance, a FE model of the system can be updated based on the modal testing data [Ewi84, Fri95]. The orthogonality property of the eigenvectors in Lemma 4.2 can still be ensured from this updating method. Hence, the proposed FE approach can also be used for such models.

5.9 Summary

We extended the methodology for optimal placement of actuators by introducing an extra constraint for control spillover reduction. In addition, we proposed a new methodology for finding optimal placement of general sensors over a flexible structure. In particular, optimal placement of piezoelectric actuators and sensors were considered. The method was used for optimal placement of a collocated piezoelectric actuator/sensor pair over a thin plate, which was then tested experimentally. Finally, we extended the methodology for models that are obtained from other modelling methods such as the FE method. Therefore, optimal placement of actuators and sensors over a wide range of structures can also be dealt with by the proposed methodology.

Chapter 6

Resonant control

In the remaining three chapters, we will concentrate on the issue of designing active controllers to control vibrations of smart structures, starting with resonant controllers.

One of the characteristics of a flexible structure is its highly resonant nature. This is due to inherently small energy dissipation of kinetic and strain energy of the structure, which is reflected by a relatively small structural damping. This implies that a structure may experience considerable vibration when it is excited at frequencies at, or close to, its resonance frequencies. Excessive vibrations can be detrimental to the reliability and performance of the structure and thus need to be controlled. Realizing the highly resonant characteristic of flexible structures, we propose a class of controllers that exploit this characteristic, i.e. resonant controllers.

In other words, a resonant controller applies high gain at, or close to, resonance frequencies of interest to suppress vibration at those resonances. This type of controller is motivated by resonant controllers originally developed in [PMS99]. However, we will extend the idea to include a more general class of controllers that allows for control of multi-variable resonant systems and includes the work of [PMS99] as a special case. By appropriate design, we can implement the resonant controller in a feedback control framework to minimize vibration of structures.

Due to the highly resonant nature of the proposed controller, we expect the effect of the controller to be localized to each resonant peak. This is expected especially if the resonant peaks are sufficiently separated from one another. Hence, we can choose the resonant modes that we wish to control since it may not be necessary to control every mode.

6.1 Controller structures

Here, we propose a multivariable controller structure that is applicable to flexible structures with compatible and collocated actuators and sensors [HM01d, HM01c]. In addition, we will discuss a special type of resonant controller that has good robustness properties when implemented on collocated systems. In this section we concentrate on piezoelectric laminate structures.

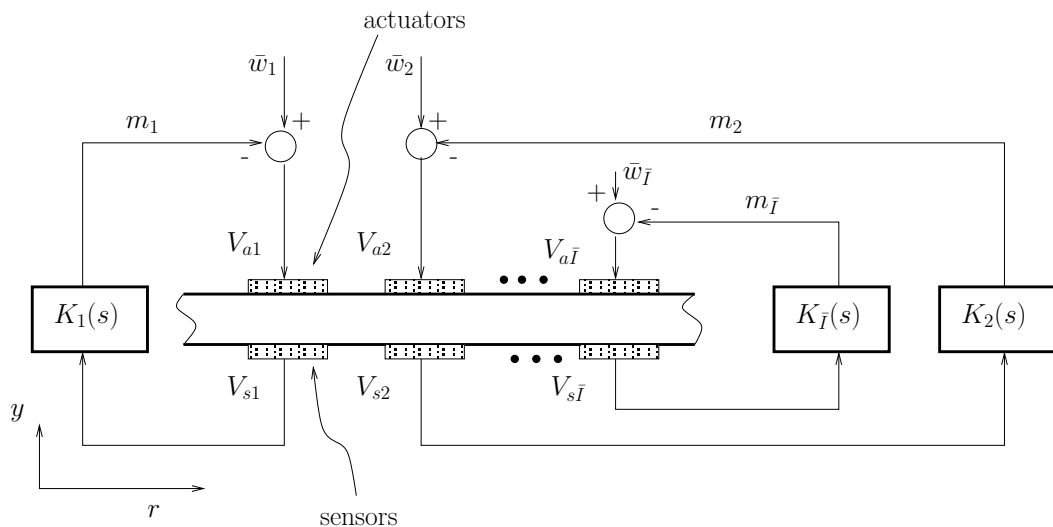


Figure 6.1: A flexible structure with collocated actuator/sensor pairs

Consider a flexible structure with a number of piezoelectric actuator/sensor pairs attached to it as shown in Figure 6.1. Suppose there are \bar{I} collocated actuator/sensor pairs distributed along the structure. Piezoelectric patches on one side of the beam are used as sensors, while patches on the other side serve as actuators. The actuator voltage is $V_a = [V_{a1} \dots V_{a\bar{I}}]^T$, while the sensor voltage

is $V_s = [V_{s1} \dots V_{s\bar{I}}]^T$. The controller output voltage is $m = [m_1 \dots m_{\bar{I}}]^T$, while the external disturbance is $\bar{w} = [\bar{w}_1 \dots \bar{w}_{\bar{I}}]^T$.

The system has a collocated nature whose transfer function can be shown to be as in (2.89). We consider $\Upsilon_i = c_i P_i^T$ with $c_i > 0$, so $\Upsilon_i P_i \geq 0$. Here, we use the truncated version of G_{V_s} (2.89):

$$G_{V_s}^M(s) = \sum_{i=1}^M \frac{c_i P_i^T P_i}{s^2 + 2\zeta_i \omega_i s + \omega_i^2} \quad (6.1)$$

where $M \gg N$ and N is the highest resonant mode that is to be controlled. The task is to design a decentralized controller K to control structural vibration due to a number of modes of interest.

As mentioned previously, considerable vibration of a flexible structure occurs when it is excited at a frequency at or near its resonance frequencies. Hence, we can suppress structural vibration due to a particular mode by minimizing the resonant response of that mode. We design a feedback controller with a particular structure that applies high gain at the resonance frequency. By careful design, we can suppress structural vibration due to that mode by implementing the feedback controller.

We consider again the control system in Figure 6.1. The l^{th} actuator/sensor pair is controlled independently by the controller K_l . The measured voltages from the piezoelectric sensors V_s act as the input to the controller. The controller applies voltages m to the piezoelectric actuators. The external disturbance \bar{w} is assumed to enter the system through the actuators.

We extend the resonant controller proposed in [PMS99] to include a more general class of resonant controllers. The proposed decentralized resonant controller is

$$K(s) = \text{diag}(K_1(s) \ K_2(s) \ \dots \ K_{\bar{I}}(s)) \quad (6.2)$$

where

$$K_l(s) = \sum_{i=1}^N \left(\frac{\alpha_{li} s (s + 2d_{li} \omega_i)}{s^2 + 2d_{li} \omega_i s + \omega_i^2} + R_{li} \right), \quad l = 1, 2, \dots, \bar{I}, \quad \alpha_{li} \geq 0 \quad \forall l, i. \quad (6.3)$$

Here, N modes lie within the controlled bandwidth, and out of these modes $N_c \leq N$ modes are to be controlled. The term α_{li} is the i^{th} modal gain of the controller for the l^{th} actuator/sensor pair and R_{li} is a feedthrough term. If a particular mode is not to be controlled, then α_{li} corresponding to that mode is set to zero for all l . The resonant controller structure proposed in [PMS99] can be shown to be a special case of our resonant controller structure when $R_{li} = 0$ for all i and $l = 1$, i.e. a SISO controller. Our proposed structure involves a more general case of resonant controllers, with R_{li} not necessarily zero for all l and i . This leads to a more flexible choice for finding the optimal controller for vibration control.

This resonant controller can be designed and implemented to suppress structural vibration. However, the robustness of the controller needs to be ensured first before it is implemented. This is important since the model used always contains some degree of uncertainty. In general, we can design the controller and check the robustness of the controller afterwards.

However, there is a special case of these resonant controllers that has an inherent robustness against parametric uncertainties and unmodelled dynamics. The parametric uncertainties may involve the uncertainties in determining the resonance frequency and damping associated with each mode. The uncertainties in unmodelled dynamics occur since the model may only include the in-bandwidth modes, neglecting the dynamics of out-of-bandwidth modes. Hence, the controller may undesirably sense/excite higher frequency modes, which may result in instability and performance reduction once implemented on the real systems. This problem is referred to as the spillover effect [Bal78a, Bal78b]. Next, we consider a type of robust resonant controller.

6.1.1 Robust resonant controller

We consider a particular type of the resonant controller structure. This is the special case of resonant controllers in (6.3) with $R_{li} = 0 \quad \forall l, i$.

$$K(s) = \text{diag}(K_1(s) \quad K_2(s) \dots K_{\bar{l}}(s)) \quad (6.4)$$

where

$$K_l(s) = \sum_{i=1}^N \frac{\alpha_{li} s (s + 2d_{li} \omega_i)}{s^2 + 2d_{li} \omega_i s + \omega_i^2}, \quad l = 1, 2, \dots, \bar{l}, \quad \alpha_{li} \geq 0 \quad \forall l, i. \quad (6.5)$$

We will show that this type of resonant controller guarantees closed-loop stability in the presence of parametric and unmodelled dynamics uncertainties.

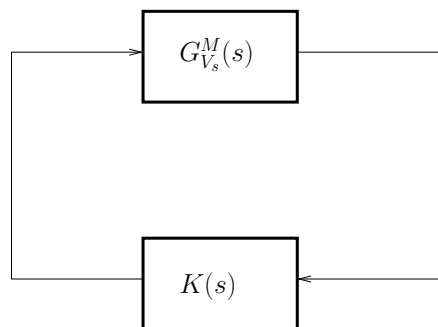


Figure 6.2: A feedback system

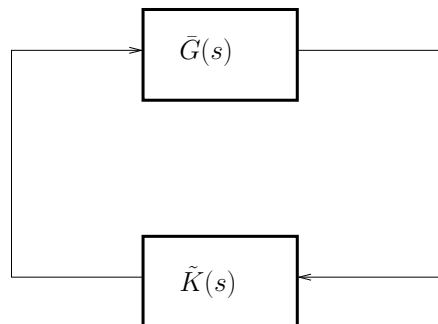


Figure 6.3: An equivalent feedback system

Consider the negative feedback connection shown in Figure 6.2. Here, we assume that $K(s)$ has a structure defined by (6.4) and (6.5). We work with a finite-dimensional model $G_{V_s}^M$ (6.1) since we intend to use stability results that are applicable to finite-dimensional LTI systems. It is acceptable to work with a truncated version of G_{V_s} (2.89) since the transfer function rolls off at higher frequencies [Hug87]. Therefore, for a large enough M , the stability results will extend to the full infinite-dimensional model of the system.

To prove closed-loop stability of the negative feedback loop in Figure 6.2, we consider the equivalent feedback system shown in Figure 6.3 where

$$\bar{G}(s) = s G_{V_s}^M(s) \quad (6.6)$$

and

$$\tilde{K}(s) = \frac{K(s)}{s}. \quad (6.7)$$

Here, \bar{G} can be seen as the transfer function from the actuator voltage to the rate of change of the sensor voltage.

We can show that \bar{G} is a positive-real transfer function since $\bar{G}(j\omega) + \bar{G}(j\omega)^*$ is positive-semidefinite for all $\omega \in \mathbf{R}$. That is

$$\begin{aligned} \bar{G}(j\omega) + \bar{G}(j\omega)^* &= \sum_{i=1}^M \left(\frac{c_i P_i^T P_i j\omega}{(\omega_i^2 - \omega^2) + 2\zeta_i \omega_i j\omega} + \frac{-c_i P_i^T P_i j\omega}{(\omega_i^2 - \omega^2) - 2\zeta_i \omega_i j\omega} \right) \\ &= \sum_{i=1}^M \frac{4c_i P_i^T P_i \zeta_i \omega_i \omega^2}{(\omega_i^2 - \omega^2)^2 + (2\zeta_i \omega_i \omega)^2} \\ &\geq 0 \quad \omega \in \mathbf{R}. \end{aligned} \quad (6.8)$$

Having established the positive-realness of \bar{G} , closed-loop stability follows if we can show that \tilde{K} is strictly positive-real in the weak sense. Following [JG96], a stable square transfer function matrix \tilde{K} is strictly positive-real in the weak sense if $\tilde{K}(j\omega) + \tilde{K}(j\omega)^* > 0$ for $\omega \in (-\infty, \infty)$.

Noticing that \tilde{K} is diagonal, we only need to consider its diagonal elements:

$$\begin{aligned}\tilde{K}_i(j\omega) + \tilde{K}_l(j\omega)^* &= \sum_{i=1}^N \left\{ \alpha_{li} \left(\frac{j\omega + 2d_{li}\omega_i}{(\omega_i^2 - \omega^2) + 2d_{li}\omega_i j\omega} + \frac{-j\omega + 2d_{li}\omega_i}{(\omega_i^2 - \omega^2) - 2d_{li}\omega_i j\omega} \right) \right\} \\ &= \sum_{i=1}^N \frac{4\alpha_{li}d_{li}\omega_i^3}{(\omega_i^2 - \omega^2)^2 + (2d_{li}\omega_i\omega)^2} \\ &> 0, \quad \omega \in (-\infty, \infty), \quad l = 1, 2, \dots, \bar{I}.\end{aligned}\tag{6.9}$$

This implies that $\tilde{K}(j\omega) = \text{diag}(\tilde{K}_1(j\omega) \dots \tilde{K}_{\bar{I}}(j\omega)) > 0$ for $\omega \in (-\infty, \infty)$. Therefore, using Corollary 1.1 of [JG96], the negative feedback connection of \tilde{K} and \bar{G} is stable. Hence, the negative feedback connection of Figure 6.2 is also stable.

The positive-realness of \bar{G} is ensured by collocating compatible actuators and sensors. Hence, any controller K with $\tilde{K}(s) = K(s)/s$ such that \tilde{K} is strictly positive-real in the weak sense will ensure closed-loop stability.

Therefore, the class of controllers defined by (6.4) and (6.5) are robustly stable with respect to incorrect resonance frequencies and damping ratios. The closed-loop stability is also guaranteed in the presence of high frequency and in-bandwidth modes that are left uncontrolled. If the resonance frequencies and damping ratios of the model are incorrect, the controller will not destabilize the closed-loop system. However, the controller may not be able to perform optimally.

In the next section, we will determine controller parameters of the general resonant controllers in (6.2) and (6.3) via an optimization procedure.

6.2 Optimization for resonant controllers

To design our proposed resonant controller, three parameters for each mode are needed, i.e. α_{li} , d_{li} and R_{li} . These parameters can be determined in a fairly simple way for a SISO system, since it can be done by trial and error. However, a more systematic method is desirable for multivariable systems, which will be discussed in this section.

From (6.3), the controller $K(s)$ is parameterized in terms of α_{li} , d_{li} and R_{li} . Therefore, any optimization has to be carried out over these parameters. Among these parameters, the damping ratio has a considerable role in determining the achievable vibration reduction of its associated mode. This is because the system has a resonant nature and the controller only needs to apply high gain at frequencies at, or close to, the system resonances. Choosing a smaller damping ratio would lead to higher gain applied to the corresponding resonance, which is desirable. However, the damping ratio need to be carefully optimized since an inappropriate damping ratio may even increase the response at frequencies around the resonance. Hence, our approach here is to concentrate on choosing a set of parameters α_{li} and R_{li} first and then optimize over d_{li} . Later, it will be shown that it is reasonable to use α_{li} that is obtained from a single-mode controller, assuming the resonant peaks of interest are sufficiently separated from one another.

We consider systems G in (2.83) and G_{V_s} in (2.89). As a reminder, G is the transfer function from the actuator output to the structural deflection at any location r along the structure. The truncated version of G and G_{V_s} can be written in state-space form:

$$\begin{aligned}\dot{x}_b(t) &= \begin{bmatrix} 0 & I \\ -W_b^2 & -2Z_bW_b \end{bmatrix} x_b(t) + \begin{bmatrix} 0 \\ H \end{bmatrix} \bar{w}(t) \\ y(t, r) &= [U_d(r) \quad 0] x_b(t) \\ V_s(t) &= [U \quad 0] x_b(t)\end{aligned}\tag{6.10}$$

where

$$\begin{aligned}Z_b &= \text{diag}(\zeta_1 \dots \zeta_M) \\ W_b &= \text{diag}(\omega_1 \dots \omega_M) \\ H &= [P_1^T \dots P_M^T]^T \\ U &= [c_1 P_1^T \dots c_M P_M^T] \\ U_d(r) &= [\phi_1(r) \dots \phi_M(r)]\end{aligned}\tag{6.11}$$

and the number of modes considered in the truncated model is M . The state x_b is $[q_1 \dots q_M \quad \dot{q}_1 \dots \dot{q}_M]^T$.

For a MIMO system, each independent controller K_l in (6.3) can be written in its state-space form as:

$$\begin{aligned}\dot{\hat{x}}_l(t) &= \begin{bmatrix} 0 & I \\ -W_c^2 & -2D_l W_c \end{bmatrix} \hat{x}_l(t) + \begin{bmatrix} 0 \\ X_l \end{bmatrix} V_{sl}(t) \\ m_l(t) &= [Y_l \quad 0] \hat{x}_l(t) + Z_l V_{sl}(t).\end{aligned}\quad (6.12)$$

If we order the vibration modes that are to be controlled as n_1, \dots, n_{N_c} , where N_c is the number of modes to be controlled, we can define $D_l = \text{diag}(d_{ln_1} \dots d_{ln_{N_c}})$, $W_c = \text{diag}(\omega_{n_1} \dots \omega_{n_{N_c}})$ and $\hat{x}_l = [\hat{q}_{ln_1} \dots \hat{q}_{ln_{N_c}} \quad \dot{\hat{q}}_{ln_1} \dots \dot{\hat{q}}_{ln_{N_c}}]^T$. The terms X_l, Y_l and Z_l can also be obtained in a straightforward manner from (6.3).

We then combine all independent controllers to obtain the MIMO controller:

$$\begin{aligned}\dot{\hat{x}}(t) &= \begin{bmatrix} 0 & I \\ -\tilde{W}^2 & -2\tilde{D}\tilde{W} \end{bmatrix} \hat{x}(t) + \begin{bmatrix} 0 \\ X \end{bmatrix} V_s(t) \\ m(t) &= [Y \quad 0] \hat{x}(t) + Z V_s(t)\end{aligned}\quad (6.13)$$

where $m = [m_1 \dots m_{\bar{I}}]^T$ is the output voltage from the controller and

$$\begin{aligned}\tilde{W} &= \text{diag}(W_c \dots W_c) \\ \tilde{D} &= \text{diag}(D_1 \dots D_{\bar{I}}) \\ X &= \text{diag}(X_1 \dots X_{\bar{I}}) \\ Y &= \text{diag}(Y_1 \dots Y_{\bar{I}}) \\ Z &= \text{diag}(Z_1 \dots Z_{\bar{I}}).\end{aligned}\quad (6.14)$$

Moreover, the controller states follow from ordering the states of all independent controllers as:

$$\hat{x} = [\hat{q}_{1n_1} \quad \hat{q}_{1n_2} \dots \hat{q}_{\bar{I}n_{(N_c-1)}} \quad \hat{q}_{\bar{I}n_{N_c}} \quad \dot{\hat{q}}_{1n_1} \quad \dot{\hat{q}}_{1n_2} \dots \dot{\hat{q}}_{\bar{I}n_{(N_c-1)}} \quad \dot{\hat{q}}_{\bar{I}n_{N_c}}]^T. \quad (6.15)$$

The closed-loop system can then be obtained from (6.10) and (6.13):

$$\begin{aligned}\dot{\bar{x}}(t) &= \bar{A}\bar{x}(t) + \bar{B}\bar{w}(t) \\ y(t, r) &= \bar{C}_d(r)\bar{x}(t) \\ V_s(t) &= \bar{C}\bar{x}(t)\end{aligned}\tag{6.16}$$

where $\bar{x} = [x_b^T \quad \hat{x}^T]^T$ and

$$\begin{aligned}\bar{A} &= \begin{bmatrix} 0 & I & 0 & 0 \\ -W_b^2 - HZU & -2Z_bW_b & -HY & 0 \\ 0 & 0 & 0 & I \\ XU & 0 & -\tilde{W}^2 & -2\tilde{D}\tilde{W} \end{bmatrix} \\ \bar{B} &= [0 \quad H^T \quad 0 \quad 0]^T \\ \bar{C} &= [U \quad 0 \quad 0 \quad 0] \\ \bar{C}_d(r) &= [U_d(r) \quad 0 \quad 0 \quad 0].\end{aligned}\tag{6.17}$$

We wish to parameterize the closed-loop system (6.16) in terms of controller damping ratios d_{li} for fixed values of α_{li} . For this purpose, \bar{A} can be represented as a finite sum:

$$\bar{A} = A - 2 \sum_{l=1}^{\bar{I}} \sum_{j=1}^{N_c} \omega_{n_j} d_{ln_j} E_{ln_j} E_{ln_j}^T\tag{6.18}$$

where A is independent of damping ratio d_{li} .

Here, the use of i and n_j should not be confused since n_j is used to specify each vibration mode that is to be controlled in the optimization process. This notation is adopted here since only a limited number of in-bandwidth modes are to be controlled. For instance, $[n_1 \ n_2 \ n_3] = [1 \ 3 \ 4]$ implies that only modes $i = 1, 3$ and 4 are to be controlled. However, we will use i to signify vibration modes in the general case throughout this chapter.

Matrix E_{ln_j} is used to locate the corresponding d_{ln_j} in the matrix \bar{A} . The term E_{ln_j} associated with d_{ln_j} is defined as:

$$E_{ln_j} = \begin{bmatrix} 0_{M \times 1} \\ 0_{M \times 1} \\ 0_{(\bar{l} N_c) \times 1} \\ \bar{E}_{ln_j}{}_{(\bar{l} N_c) \times 1} \end{bmatrix} \quad (6.19)$$

where the dimensions of each matrix are defined above. Here, \bar{E}_{ln_j} consists of zero elements except for the corresponding row of d_{ln_j} , where

$$\bar{E}_{ln_j}((l-1)N_c + j, 1) = 1.$$

The optimization can be set to find the optimal d_{li} parameters. Here, we use the spatial \mathcal{H}_2 norm of the closed-loop system as the cost function to be minimized. However, other performance measures such as \mathcal{H}_2 norm can also be used. The optimization task is to determine

$$d_{li}^* = \arg \min \ll T_{y\bar{w}}(s, r) \gg_2^2 \quad (6.20)$$

where $T_{y\bar{w}}$ represents the closed-loop transfer function from disturbance \bar{w} to deflection y at every point on the structure. By solving the optimization problem, we wish to obtain a resonant controller that minimizes structural vibration in a spatially-averaged sense.

We consider the results in Chapter 3 to simplify this spatial \mathcal{H}_2 norm optimization. Theorem 3.1 implies that the spatial \mathcal{H}_2 norm of (6.16) is equivalent to the \mathcal{H}_2 norm of the finite-dimensional system:

$$\begin{aligned} \dot{\bar{x}}(t) &= \bar{A}\bar{x}(t) + \bar{B}\bar{w}(t) \\ \bar{y}(t) &= \bar{\Gamma}\bar{x}(t) \\ V_s(t) &= \bar{C}\bar{x}(t) \end{aligned} \quad (6.21)$$

where

$$\bar{\Gamma}^T \bar{\Gamma} = \int_0^L \bar{C}_d(r)^T \bar{C}_d(r) dr. \quad (6.22)$$

Hence, the optimization problem from (6.20) can be shown to be:

$$\begin{aligned} \min \quad & \text{tr}(\bar{B}^T L_o \bar{B}) \\ \text{subject to: } & \bar{A}^T L_o + L_o \bar{A} + \bar{\Gamma}^T \bar{\Gamma} = 0 \end{aligned} \quad (6.23)$$

where \bar{A} depends on d_{li} via (6.18).

For a fixed value for α_{li} , it is not possible to make the cost function arbitrarily small. If $d_{li} \rightarrow \infty$, it can be shown that the controller in (6.3) reduces to a simple gain. Hence, the only way that the cost function can be made arbitrarily small, is by making α_{li} arbitrarily large. This may yield a controller with excessive gain, which is not desirable. The cost function can be reduced more effectively by optimizing the damping ratios.

We introduce a matrix of Lagrange multipliers S to solve this constrained optimization problem. The Lagrangian is formed by incorporating (6.18):

$$\begin{aligned} L &= \text{tr}(\bar{B}^T L_o \bar{B}) + \text{tr}(\bar{A}^T L_o + L_o \bar{A} + \bar{\Gamma}^T \bar{\Gamma}) S \\ &= \text{tr}(\bar{B}^T L_o \bar{B}) + \text{tr} \left\{ A^T L_o S + L_o A S + \bar{\Gamma}^T \bar{\Gamma} S \right. \\ &\quad \left. - 2 \sum_{l=1}^{\bar{I}} \sum_{j=1}^{N_c} \omega_{n_j} d_{ln_j} E_{ln_j} E_{ln_j}^T L_o S \right. \\ &\quad \left. - 2 L_o \sum_{l=1}^{\bar{I}} \sum_{j=1}^{N_c} \omega_{n_j} d_{ln_j} E_{ln_j} E_{ln_j}^T S \right\} \end{aligned} \quad (6.24)$$

To obtain the first-order necessary conditions for optimality, we need to take derivatives of the Lagrangian L with respect to parameters L_o , S and d_{ln_j} . Hence, setting these derivatives to zero gives

$$\frac{\partial L}{\partial L_o} = \bar{B} \bar{B}^T + \bar{A} S + S \bar{A}^T = 0 \quad (6.25)$$

$$\frac{\partial L}{\partial S} = \bar{A}^T L_o + L_o \bar{A} + \bar{\Gamma}^T \bar{\Gamma} = 0 \quad (6.26)$$

$$\begin{aligned} \frac{\partial L}{\partial d_{ln_j}} &= -4 \omega_{n_j} E_{ln_j}^T L_o S E_{ln_j} = 0, \\ j &= 1, 2, \dots, N_c \quad l = 1, 2, \dots, \bar{I} \end{aligned} \quad (6.27)$$

These equations (6.25), (6.26), and (6.27) have to be solved simultaneously to satisfy the optimality condition of the spatial \mathcal{H}_2 norm of the system. Since the

closed-form solution is not possible, a numerical approach is used instead. The form given in (6.27) can be used as the gradient to obtain a local minimum of the function.

We will summarize the above optimization procedure as follows. The modal gains α_{li} and R_{li} are set at some specific levels to obtain a sufficient reduction of each resonant response. It is, however, possible to optimize over α_{li} and R_{li} as well as d_{li} . The value R_{li} will determine the feedthrough term of the controller. The selection of modal gains will be discussed in the next section. An initial guess for each controller damping ratio d_{li} (or its corresponding d_{ln_j}) is made. Any positive d_{li} can be used as a starting point since that would guarantee stability.

Matrices \bar{B} and $\bar{\Gamma}$ only need to be calculated once since they are independent of damping d_{li} . Matrix \bar{A} is obtained from (6.18), while the observability and controllability Gramian matrices L_o and S are calculated by solving the Lyapunov equations in (6.25) and (6.26). The gradient for each value of damping d_{li} is calculated from (6.27). The process is iterated by updating the damping ratio d_{li} until a solution with acceptable accuracy is obtained. Furthermore, since the optimization problem is non-convex in general, the iterative optimization procedure can be carried out for a number of initial guesses, and then the best solution can be used.

We will explore the optimization in more detail in the next section. The use of the optimization to design a resonant controller for a piezoelectric laminate beam will also be demonstrated.

6.3 Resonant control of a piezoelectric laminate beam

Here, we design and implement a resonant controller for minimizing vibration of a piezoelectric laminate structure. The structure is a simply-supported beam

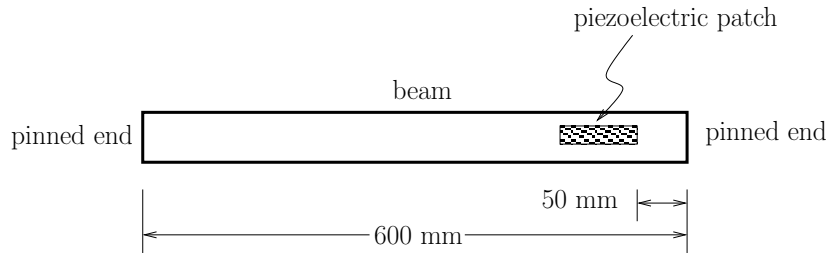


Figure 6.4: A piezoelectric laminate beam

with a collocated piezoelectric actuator/sensor pair attached to either side of it (Figure 6.4). The structure used is similar to the one described in Section 4.4. The piezoceramic elements used in our experiment are PIC151 patches. The properties of the structure and PIC151 can be found in Table 4.2.

Modal analysis is used to obtain a model of the structure. The model is truncated by keeping the first 10 structural modes, i.e. $M = 10$. The model correction approach, explained in Chapter 4, is used in our model. In this approach, we add feedthrough terms $D_d(r)$ and D_{V_s} to the system outputs in (6.10):

$$\begin{aligned}
 \dot{x}_b(t) &= A_d x_b(t) + B_d \bar{w}(t) \\
 y(t, r) &= C_d(r) x_b(t) + D_d(r) \bar{w}(t) \\
 V_s(t) &= C_{V_s} x_b(t) + D_{V_s} \bar{w}(t)
 \end{aligned} \tag{6.28}$$

where A_d, B_d, C_d and C_{V_s} are defined from the system in (6.10).

We can rely on experiments to estimate a feedthrough term such as D_{V_s} . However, the estimation of feedthrough term $D_d(r)$ is not straightforward since it is a function of spatial location r . Furthermore, a numerical spatial integration will be needed to calculate the system spatial \mathcal{H}_2 norm (6.22). Thus, we decide to use the method explained in Chapter 4 to determine $D_d(r)$.

The feedthrough term $D_d(r)$ is calculated to minimize the spatial \mathcal{H}_2 norm of the error between the infinite-dimensional model and the corrected model,

assuming the system damping is small. The assumption is reasonable since based on our experiments, the damping ratio associated with each mode is in the order of 0.01 or 0.001. Hence,

$$D_d(r) = \sum_{i=M+1}^{M_a} \phi_i(r) K_{r_i}^{opt} \quad (6.29)$$

where mode M_a is the highest out-of-bandwidth mode considered and $K_{r_i}^{opt}$ is as in (4.16):

$$K_{r_i}^{opt} = \frac{1}{2\omega_{co}\omega_i} \ln \left(\frac{\omega_i + \omega_{co}}{\omega_i - \omega_{co}} \right) P_i. \quad (6.30)$$

Here, ω_{co} lies within the interval $\omega_{co} \in (\omega_M, \omega_{M+1})$ and $P_i = K_1 \Psi_{i1}$, where Ψ_{k1} is defined in (2.81). The above term is calculated by considering modes $M + 1$ to $M_a = 200$ to obtain a sufficient approximation to the feedthrough term.

However, adding feedthrough terms into the system implies that the spatial \mathcal{H}_2 norm from the input to output y will not be finite. To avoid this problem, we absorb the effect of feedthrough terms into the dynamics of the system by adding second-order out-of-bandwidth terms as suggested in [Cla97]. The second-order term has the form of

$$\frac{\alpha_c(r)}{s^2 + 2\zeta_c \omega_c s + \omega_c^2}$$

where gain $\alpha_c(r)$ is determined to ensure that the DC content of the second-order term is close to that of the system in (6.28).

The resonance frequency of the second-order system is set at $\omega_c = 16$ KHz, well above the bandwidth of interest of about 2 KHz. A relatively high damping ratio of $\zeta_c = 0.7$ is used so that the second-order system behaves like a low-pass filter. Since the controller and the system are highly resonant, this addition will have minimal effect on the optimization result. This will make the optimization procedure feasible, and will not increase the controller bandwidth.

The modified system after the inclusion of the second-order mode to the system can be shown to be:

$$\tilde{A}_d = \begin{bmatrix} 0_{(M+1) \times (M+1)} & I_{(M+1) \times (M+1)} \\ \tilde{A}_{d1_{(M+1) \times (M+1)}} & \tilde{A}_{d2_{(M+1) \times (M+1)}} \end{bmatrix}$$

where dimensions of each matrix are defined accordingly and

$$\begin{aligned}\tilde{A}_{d1} &= -\text{diag}(\omega_1^2 \dots \omega_M^2 \ \omega_c^2) \\ \tilde{A}_{d2} &= -2 \text{diag}(\zeta_1 \omega_1 \dots \zeta_M \omega_M \ \zeta_c \omega_c).\end{aligned}$$

Moreover,

$$\begin{aligned}\tilde{B}_d &= [0 \dots 0 \ 0 \ K_1 \Psi_{11} \dots K_1 \Psi_{M1} \ 1]^T \\ \tilde{C}_d(r) &= [\phi_1(r) \dots \phi_M(r) \ \omega_c^2 \sum_{i=M+1}^{M_a} K_{ri}^{opt} \phi_i(r) \ 0 \ \dots 0 \ 0] \\ \tilde{C}_{Vs} &= [\Omega_1 \Psi_{11} \dots \Omega_1 \Psi_{M1} \ D_{Vs} \omega_c^2 \ 0 \dots 0 \ 0]\end{aligned}\quad (6.31)$$

where $\tilde{A}_d, \tilde{B}_d, \tilde{C}_d$ and \tilde{C}_{Vs} signify the modified system of A_d, B_d, C_d and C_{Vs} that are defined in (6.10).

The closed-loop system in (6.21) can be constructed from (6.13) and (6.31). Here, $\bar{\Gamma}$ in (6.22) is calculated by taking advantage of the orthogonality property of eigenfunctions ϕ_i in (3.6):

$$\bar{\Gamma} = \begin{bmatrix} \tilde{\Gamma} & 0 \\ 0 & 0 \end{bmatrix}\quad (6.32)$$

where $\tilde{\Gamma} = \text{diag} \left(1 \dots 1 \ \omega_c^2 \left(\sum_{i=M+1}^{M_a} (K_{ri}^{opt})^2 \right)^{\frac{1}{2}} \right)$.

As mentioned previously, one of the advantages of this particular controller structure is that we can choose the resonant modes that need to be controlled. For this particular beam, the placement of the piezoelectric actuator/sensor pair on the beam (see Figure 6.4) results in relatively low control authority over the first resonant mode (at a frequency of about 20 Hz). The low control authority of this mode is reflected in the frequency response (actuator voltage to sensor voltage) shown in Figure 6.11, that also reflects the low sensing authority of the collocated sensor. Thus, more control effort is needed to dampen the first mode than to control modes 2 and 3, for instance.

In this experiment, we will demonstrate the effectiveness of the controller in controlling some specific resonant modes. We attempt to control only selected modes, modes 2 and 3, and will leave the first mode uncontrolled, i.e. $\alpha_{11} = 0$.

To demonstrate our proposed controller, we choose a particular SISO resonant controller, i.e. $l = 1$:

$$\begin{aligned} K(s) &= \sum_{i=1}^3 \left(\frac{\alpha_{li} s (s + 2d_{li} \omega_i)}{s^2 + 2d_{li} \omega_i s + \omega_i^2} - \alpha_{li} \right) \\ &= \sum_{i=1}^3 \frac{-\alpha_{li} \omega_i^2}{s^2 + 2d_{li} \omega_i s + \omega_i^2}, \quad l = 1, \quad \alpha_{11} = 0. \end{aligned} \quad (6.33)$$

This particular resonant controller does not contain a feedthrough term since we choose $R_{li} = -\alpha_{li}$.

Next, we need to determine modal gain α_{li} and damping ratio d_{li} for each mode. Our approach is to select the modal gains first and to optimize the damping ratios afterwards. For this purpose, it is important to consider the effect of the modal gains on the cost function (i.e. the spatial \mathcal{H}_2 norm of the closed-loop system).

Previously, we mentioned that if the resonant peaks of the structure are sufficiently separated from each other, the controller effect tends to be localized. Hence, we can consider the case when we wish to control each mode independently, i.e. a single-mode control. By doing so, we can obtain an insight into how each modal gain affects the cost function. It will be shown later on that modal gains from single-mode control can be used as a basis for choosing modal gains for multiple-mode control. Modes 2 and 3 will be considered in our next analysis.

To analyze the effect of the modal gain, we plot the cost function versus modal gain and damping ratio for each mode. The plots for the second and third modes are shown in Figures 6.5 and 6.6 respectively. We wish to find a combination of modal gains and damping ratios that gives a sufficiently low cost function for each mode.

From Figures 6.5 and 6.6, the cost function is barely affected by the choice of damping ratio when the modal gain is less than 10^{-1} . However, when the gain is increased, a lower cost function can be achieved by increasing the damping ratio. It seems that we can reduce the cost function by increasing the modal gain and damping ratio simultaneously. Unfortunately, this is not a desirable way of

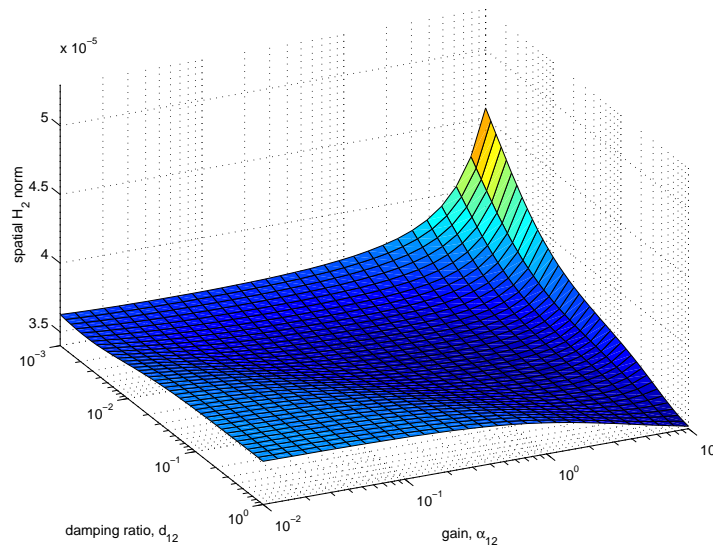


Figure 6.5: Cost function versus gain and damping ratio, mode 2

achieving our objective for vibration control. A very high gain controller is not desirable because of excessive controller effort, sensitivity to noise, and reduction of system robustness. Furthermore, a high modal gain may result in the loss of the highly localized nature of the controller. Based on these considerations and the cost function plots, we can find the sub-optimal solutions whose modal gains for the second and third modes are $\alpha_{12} = 1.5$ and $\alpha_{13} = 0.4$ respectively. These modal gains correspond to damping ratios of $d_{12} = 0.0330$ and $d_{13} = 0.0209$.

The optimization is then performed using results for single-mode control where $\alpha_{12} = 1.5$ and $\alpha_{13} = 0.4$. We use $d_{12} = 0.0330$ and $d_{13} = 0.0209$ as a starting point. A plot of the cost function versus the two damping ratios is shown in Figure 6.7. The optimal damping ratios are $d_{12} = 0.0320$ and $d_{13} = 0.0182$ as shown by the arrow in Figure 6.7. It is important to note that the damping ratios obtained here are relatively close to those obtained for single-mode controllers. This fact confirms that the effect of our resonant controller on the system is highly localized. Thus, our decision to use the modal gains obtained from the single-mode control approach is reasonable.

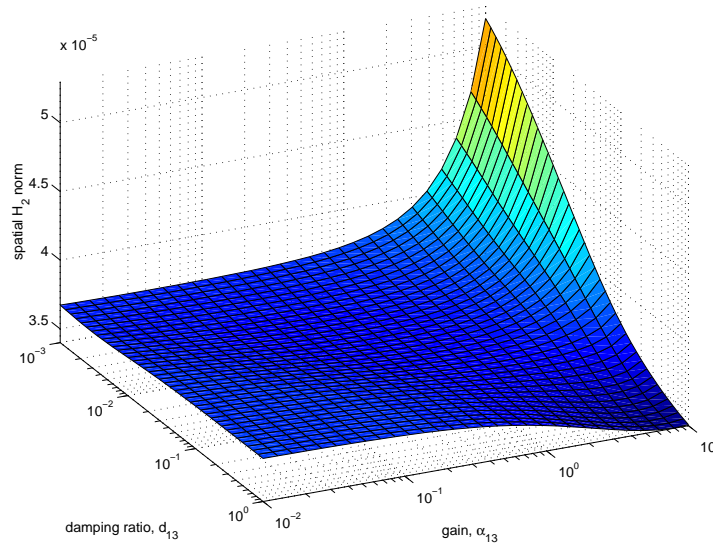


Figure 6.6: Cost function versus gain and damping ratio, mode 3

6.4 Experimental implementation

The experiment was set up at the Laboratory for Dynamics and Control of Smart Structures at the University of Newcastle, Australia. The experimental set-up is depicted in Figure 6.8, while the experimental apparatus is shown in Figure 6.9. The controller was implemented on a dSPACE DS1103 rapid prototyping Controller Board using Matlab and Simulink software. The sampling frequency was set at 20 KHz. The cut-off frequencies of the two low-pass filters were set at 10 KHz each. An HP89410A Dynamic Signal Analyzer and a Polytec PSV-300 Laser Doppler Scanning Vibrometer were used to obtain frequency responses from the piezoelectric laminate beam. The PSV-300 laser vibrometer allows accurate vibration measurement at any point on the beam. Important parameters of the beam, such as resonance frequencies and damping ratios, were obtained from the experimental apparatus and were used to correct our model.

Our simulation and experimental results are presented as follows. The frequency response of the controller is plotted in Figure 6.10. The controller has a

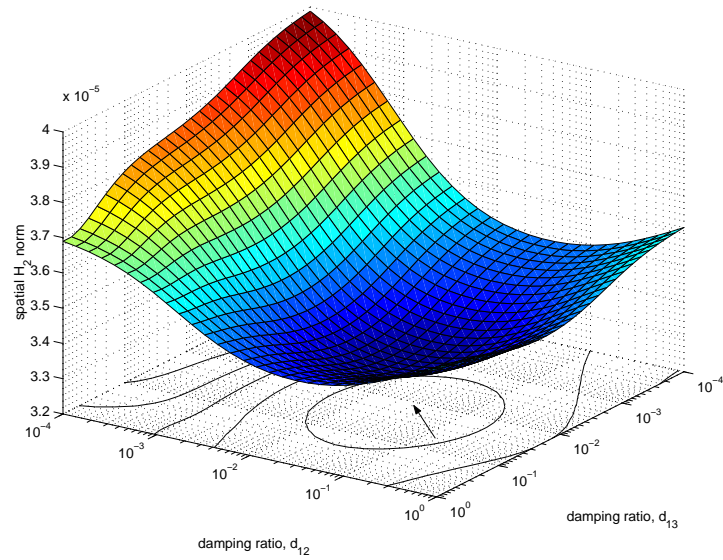


Figure 6.7: Cost function versus damping ratios

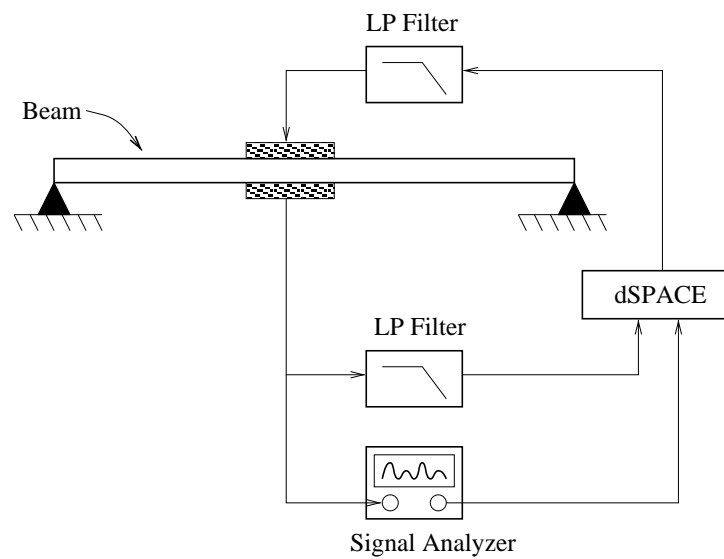


Figure 6.8: The experimental set-up



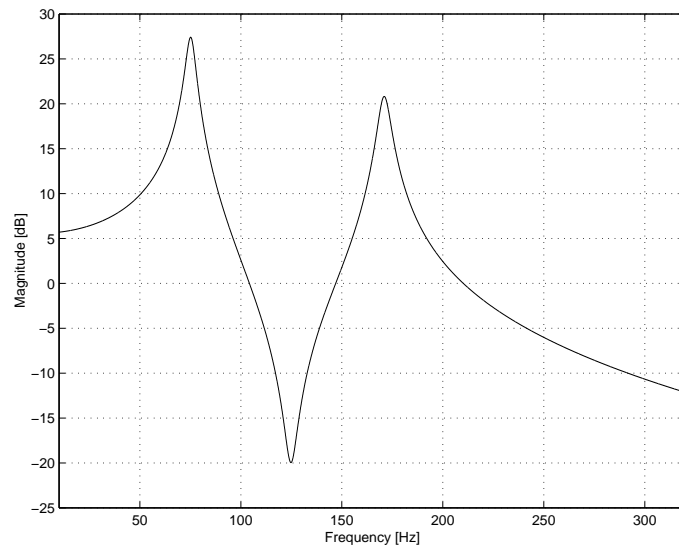
Figure 6.9: The experimental apparatus

resonant structure, as expected. Figure 6.11 compares the frequency responses (actuator voltage to sensor voltage) of the open-loop and closed-loop systems where simulation and experimental results are presented. The performance of the controller applied to the real system is as predicted by the model. The resonant responses of modes 2 and 3 of the system have been reduced significantly, while modes 1 and 4 are not affected significantly.

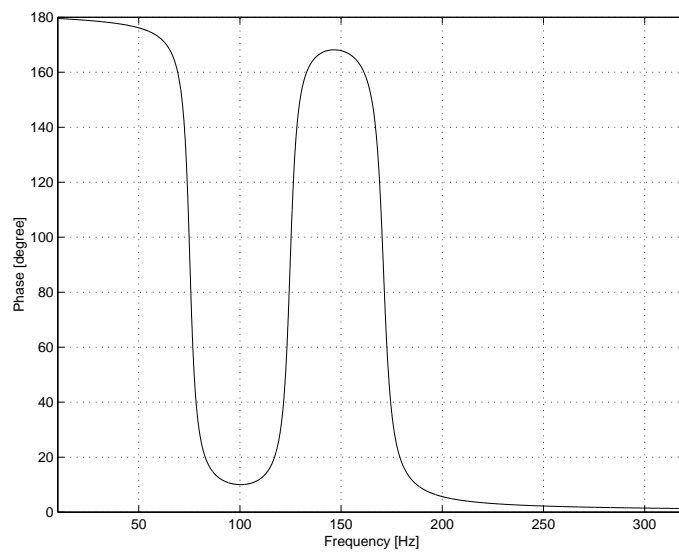
To evaluate the robustness of our controller, the experimental and simulated loop gains up to 520 Hz are shown in Figures 6.12 and 6.13. Our simulation gives a theoretical value of infinity for the gain margin and a phase margin of -35.9° at 72.1 Hz. The experiment gives a gain margin of 19.5 dB at 41.7 Hz, and a phase margin of -41.9° at 72.6 Hz. These results demonstrate sufficient robustness for our controller.

Our controller was designed to minimize the spatial \mathcal{H}_2 norm of the closed-loop system. Hence, we will demonstrate the controller effect on the vibration of the entire beam. To do this, we have plotted the spatial frequency responses of the beam.

Figures 6.14 and 6.15 show the simulated spatial frequency responses of the uncontrolled and controlled beam respectively. The location r is measured from one end of the beam, which is closer to the patches. The magnitude of the

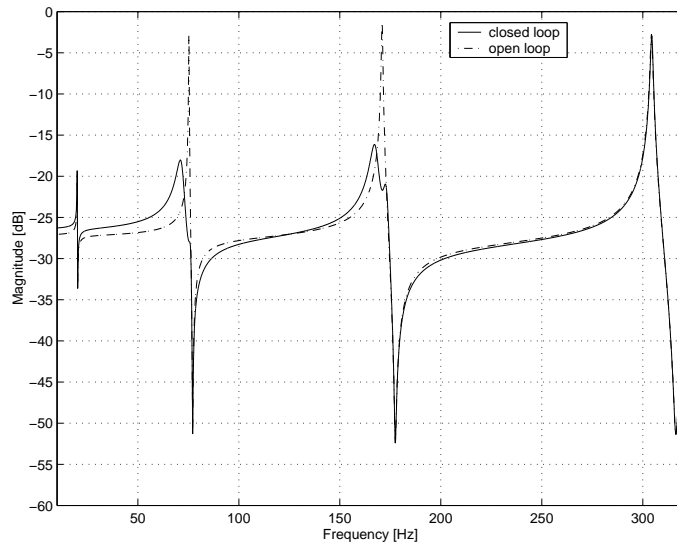


(a) magnitude

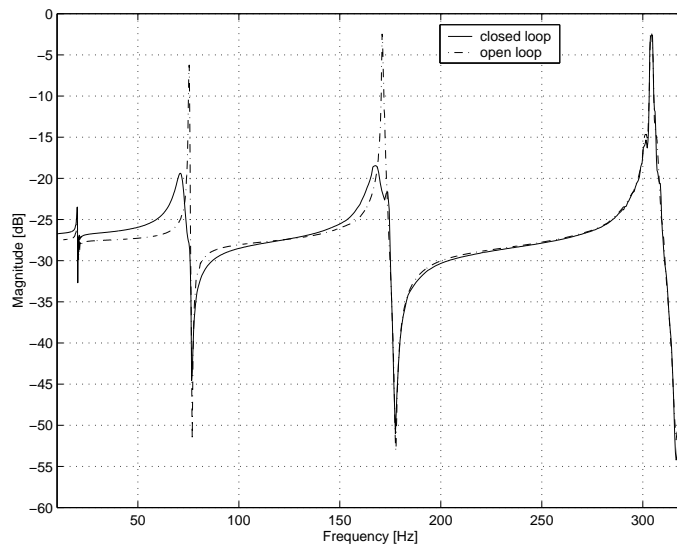


(b) phase

Figure 6.10: The frequency response of the controller (input voltage to output voltage [V/V])

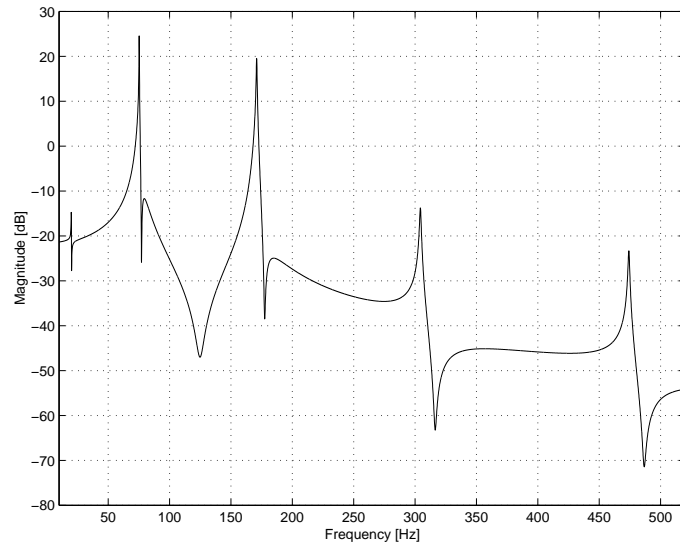


(a) simulation

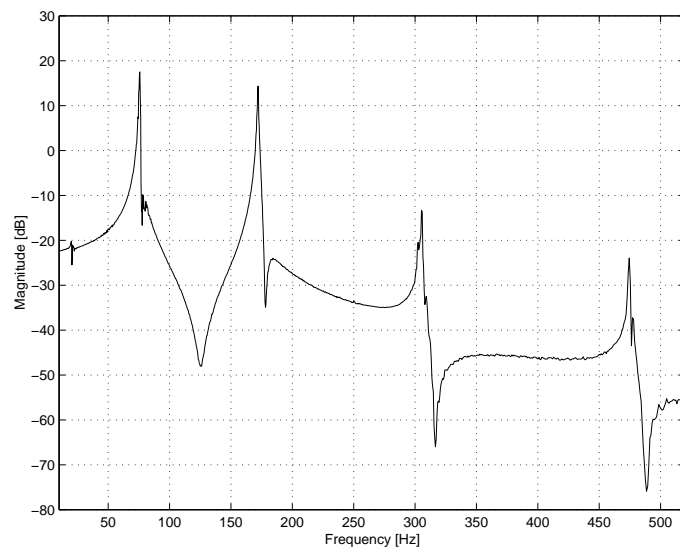


(b) experiment

Figure 6.11: Simulation and experimental frequency responses (actuator voltage to sensor voltage [V/V])

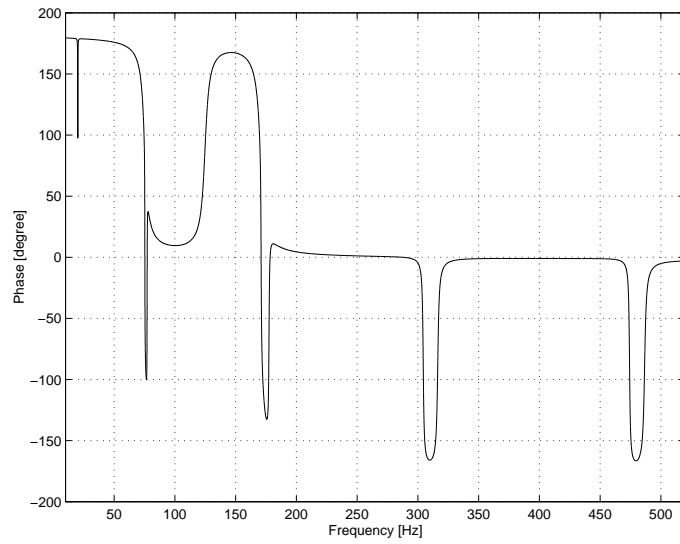


(a) simulation

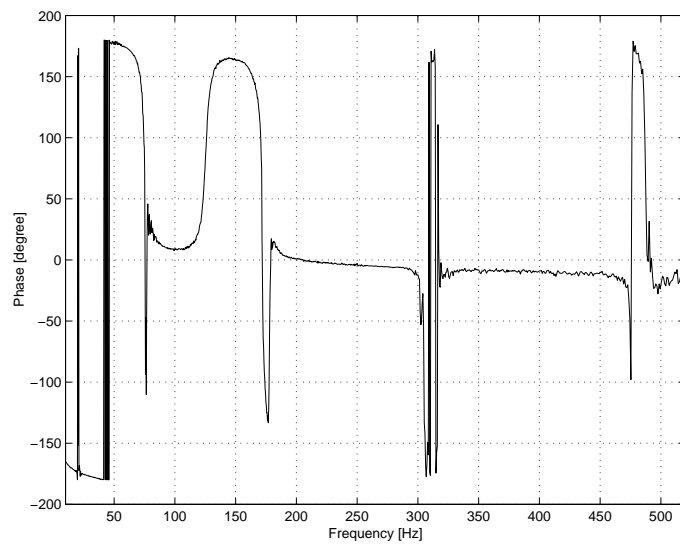


(b) experiment

Figure 6.12: Loop gain [V/V]: simulation and experiment (magnitude)



(a) simulation



(b) experiment

Figure 6.13: Loop gain [V/V]: simulation and experiment (phase)

frequency response represents the beam transverse deflection (deflection in y -axis, see Figure 6.1).

Next, a Polytec PSV-300 Laser Scanning Vibrometer was used to obtain the experimental frequency response of the beam vibration at a number of points along the beam. The results allow us to plot the spatial frequency responses of the uncontrolled and controlled beam from the experiments as shown in Figures 6.16 and 6.17 respectively. Our experiment confirms the simulation results, where we obtain vibration reduction for modes 2 and 3 over the entire structure. The experiments show that the resonant responses of modes 2 and 3 have been reduced by around 20 and 15 dB respectively, over the entire beam.

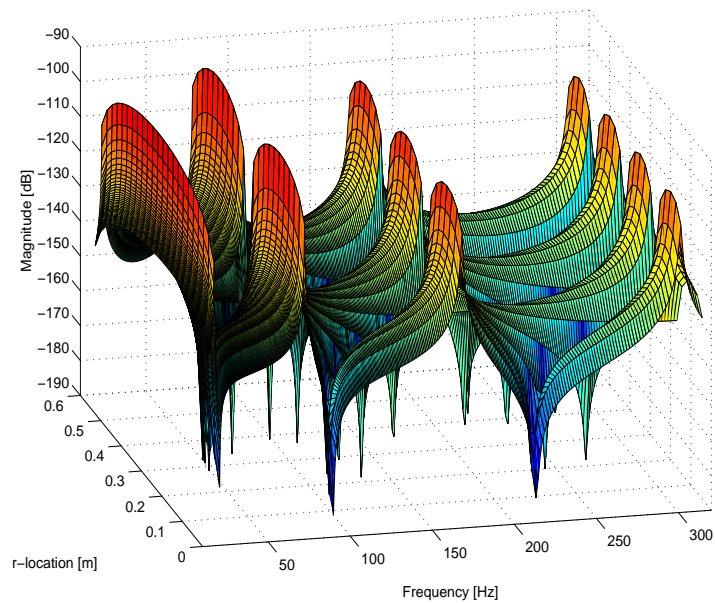


Figure 6.14: The simulated spatial frequency response: actuator voltage to beam deflection [m/V] (open loop)

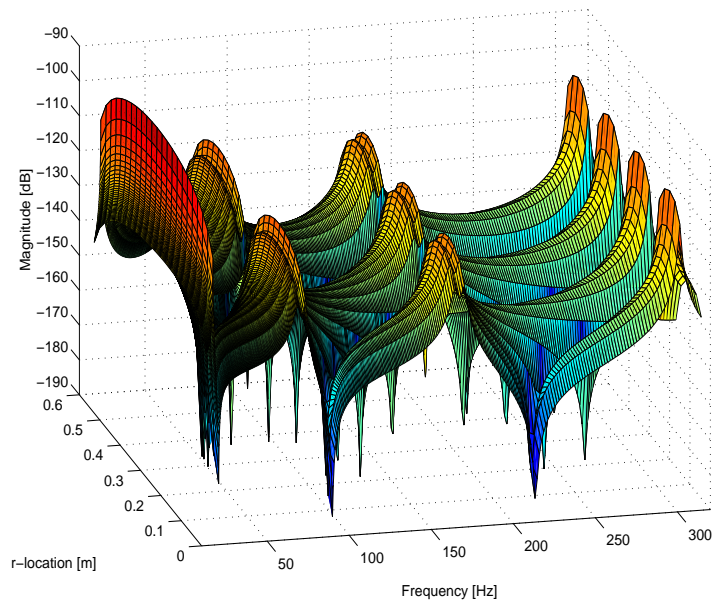


Figure 6.15: The simulated spatial frequency response: actuator voltage to beam deflection [m/V] (closed loop)

6.5 Summary

We proposed a class of resonant controllers in this chapter. These controllers can be applied to structures which contain compatible pairs of collocated actuators and sensors. The controller reduces resonant responses of the structure by applying high gain at each resonance. A special class of robust resonant controllers were introduced. The passivity of the system guarantees closed-loop stability in the presence of unmodelled dynamics and inaccurate structural models. The controller damping ratios are chosen such that the spatial \mathcal{H}_2 norm of the closed-loop system is minimized. The experiment presented shows the effectiveness of the developed controller in reducing structural vibration on a piezoelectric laminate beam.

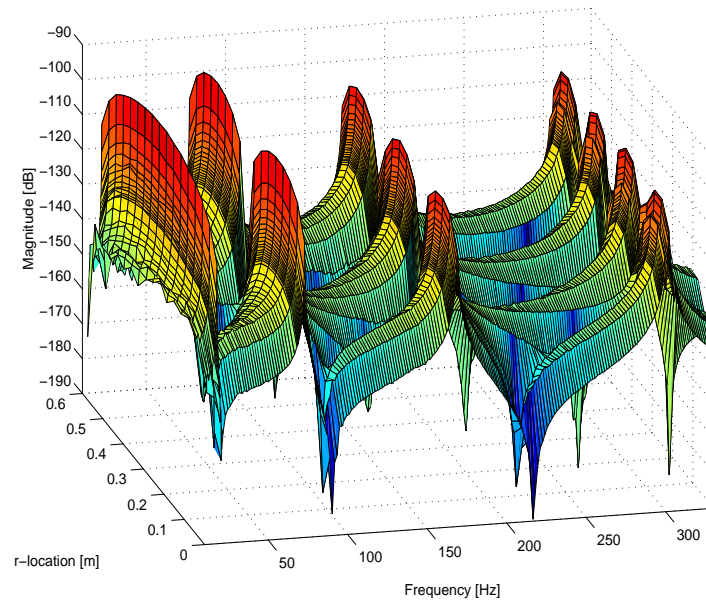


Figure 6.16: The experimental spatial frequency response: actuator voltage to beam deflection [m/V] (open loop)

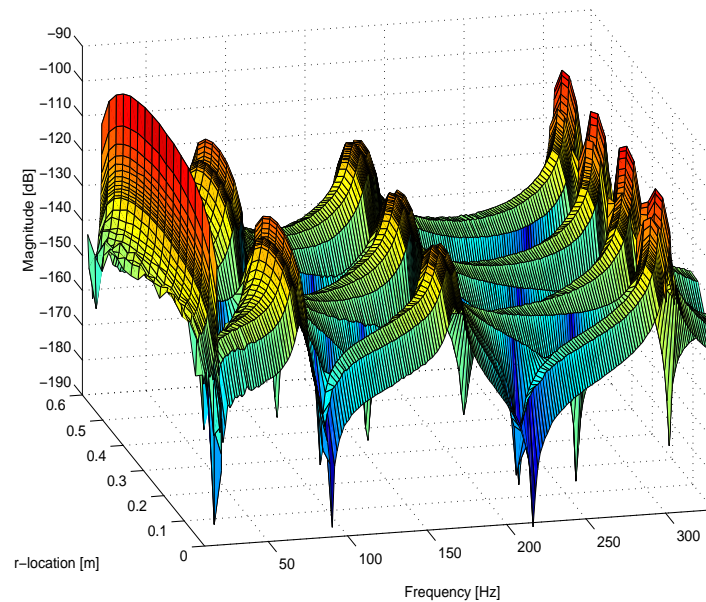


Figure 6.17: The experimental spatial frequency response: actuator voltage to beam deflection [m/V] (closed loop)